

Electro-Thermal Simulation Studies of SiC Junction Diodes Containing Screw Dislocations Under High Reverse - Bias Operation

Principal Investigator: R. P. Joshi
Department of Electrical and Computer Engineering
Old Dominion University, Norfolk, VA 23529-0246

Prepared for:
NASA Glenn Research Center
NASA Glenn Research Center, Cleveland, OH 44135.

FINAL REPORT

May, 2001.

ABSTRACT

The objective of this work was to conduct a modeling study of SiC P-N junction diodes operating under high reverse biased conditions. Analytical models and numerical simulation capabilities were to be developed for self-consistent electro-thermal analysis of the diode current-voltage (I-V) characteristics. Data from GRC [1] indicate that screw dislocations are unavoidable in large area SiC devices, and lead to changes in the SiC diode electrical response characteristics under high field conditions. For example, device instability and failures linked to internal current filamentation have been observed. The physical origin of these processes is not well understood, and quantitative projections of the electrical behavior under high field and temperature conditions are lacking. Thermal calculations for SiC devices have not been reported in the literature either. So estimates or projections of peak device temperatures and power limitations do not exist.

This numerical study and simulation analysis was aimed at resolving some of the above issues. The following tasks were successfully accomplished: (1) Development of physically based models using one- and two-dimensional drift-diffusion theory for the transport behavior and I-V characteristics. (2) One- and two-dimensional heat flow to account for internal device heating. This led to calculations of the internal temperature profiles, which in turn, were used to update the electrical transport parameters for a self-consistent analysis. The temperature profiles and the peak values were

thus obtainable for a given device operating condition. (3) Inclusion of traps assumed to model the presence of internal screw dislocations running along the longitudinal direction. (4) Predictions of the operating characteristics with and without heating as a function of applied bias with and without traps. Both one and two-dimensional cases were implemented. (5) Assessment of device stability based on the operating characteristics. The presence of internal non-uniformities, particularly filamentary structures, was probed and demonstrated. (6) Cause and physical origins of filamentary behavior and unstable I-V characteristics were made transparent. (7) It was demonstrated that diodes containing defects would be more prone to thermal breakdown associated with the temperature dependent decrease in the thermal conductivity. (8) Finally, negative differential resistance (S-shaped NDR) which can potential lead to device instability and filamentary behavior was shown to occur for diodes containing a line of defects such as could be associated with a screw dislocation line.

MODEL DETAILS

A mathematical model for the p-n SiC diode was developed on the assumption that in spite of possible internal defects and dislocations, the material can be well characterized by conduction and valance bands within the effective mass approximation. Treatment of bulk transport within the semiconductor material was based on the Drift Diffusion approach. This model relies on the assignment of effective transport parameters such as mobilities, diffusion coefficients, trap energies, trapping cross-sections, and impact ionization rates. Material parameters for SiC were taken from the published literature [2-5]. A list of the actual values used is provided in Table I. The electron and holes mobilities, $\mu_{n,p}$ respectively, were modeled by the Caughey-Thomas equation as:

$$\mu_{n,p} = \mu_{n,p}^{\min} + \mu_{n,p}^{\text{delta}} / ([1 + \{N_D + N_A\} / N_{n,p}^{\mu}]^{\gamma(n,p)}) * [T/300]^{\alpha(n,p)} \quad (1)$$

In the above, N_D and N_A are the donor and acceptor doping concentrations, "T" is the local device temperature, while the other parameters are listed in Table I. An electric field dependence to the above mobility was further included. This was done by using the following relation between $\mu_{n,p}$ and the field-dependent value $\mu_{n,p}(E)$:

$$\mu_{n,p}(E) = \mu_{n,p} [1 + \{E \mu_{n,p}\} / v_{n,p}^{\text{sat}}]^{-1/\beta(n,p)} \quad (2)$$

where $v_{n,p}^{\text{sat}}$ denote the saturation electron and hole velocities. Since the temperature changes the phonon scattering, it also affects the saturation velocity. Hence, here the following temperature dependence for the saturation velocity was used [2]:

$$v_{n,p}^{\text{sat}}(T) = v_{n,p}^{\text{sat}} / [1 + 0.8 \exp(T/300)] , \quad (3)$$

with “T” being the local temperature in degrees Kelvin. The field and temperature dependent carrier velocities $v_{n,p}(E,T)$ were obtained from (2) and (3) above with: $v_{n,p}(E,T) = E * \mu_{n,p}(E)$.

The impact ionization coefficients $\alpha_{n,p}$ were similarly taken to depend on the inverse electric field through an exponential relationship. This form was first proposed by Shockley based on a “lucky electron” model [6], and has been shown to be roughly valid for SiC [1]. However, recent experiments by Baliga et al. [7], reveal that the impact ionization coefficients, α_n and α_p change with the local temperature. Hence, both a temperature and field dependent ionization coefficients were used in the present simulations. The expressions were taken to be:

$$\alpha_n(E,T) = a_n(T) \exp[-b_n / |E|] , \quad (4a)$$

$$\text{and } \alpha_p(E,T) = a_p(T) \exp[-b_p / |E|] , \quad (4b)$$

with: $a_p(T) = 6.3 \times 10^6 - 1.07 \times 10^4 T$, and $a_n(T) = 2 \times 10^6 - 0.343 \times 10^4 T$.

A simple rectangular geometry was chosen for simplicity for the p-n junction diode with a uniform cross-section and contacts on opposite faces. The longitudinal device dimension was taken to be 5 μm (with a 1 μm P-region on the left and 4 μm N-region on the right), while the cross sectional area was chosen to be 2×10^{-9} sq. m. For numerical implementation, the entire device was spatially divided into uniform boxes. A 0.01 μm mesh was chosen along the longitudinal axis, while a 1.788 μm spacing was used in the transverse direction. The density of free carriers, ionized/unionized donors and acceptors were all represented by discrete values at the center of each box, while the internal electric fields and carrier velocities were evaluated at the edges. The time step was chosen to satisfy the requirement of being greater than both the relaxation time and the internal collision times. In order to obtain numerical stability of the space-time discretization, the well known "Courant-Fredericks-Lewy" inequality condition was used to limit the time step. The semiconductor and metal work functions were assumed to be 4.1 eV and 4.3 eV. The n-SiC material was assumed to have a donor density of $1 \times 10^{17} \text{ cm}^{-3}$ with an energy 0.075 eV below the conduction band. The p-SiC layer was taken to have an acceptor density of $1 \times 10^{18} \text{ cm}^{-3}$ and an energy level 0.2 eV above the valence band. Electron traps at a concentration of $5 \times 10^{16} \text{ cm}^{-3}$ lying at the midgap were taken to model the effects of a screw dislocation running parallel to the longitudinal axis. The width (i.e. radius in a

sense) of the screw dislocation was taken to be $3.5 \mu\text{m}$. An electron capture cross section of $5 \times 10^{14} \text{ cm}^2$ was used and is consistent with observations of predominantly electron trapping at SiC dislocation lines. For simplicity, a constant capture coefficient was assumed, though some studies indicate a field dependent trapping rate.

A two-dimensional (2D), time-dependent numerical code was then developed to implement the drift-diffusion transport model. This code developed for this study had the following salient features: (i) It was based on the drift-diffusion approach. (ii) It explicitly solved for the space- and temporal distributions of the internal electric fields and carrier densities. (iii) It yielded the self-consistent transient analysis, as well as the final steady-state response. (iv) The model was bipolar in nature, and could treat both electron and hole transport. (v) Rate equations which described the transient dynamics of the carrier generation, trapping and recombination, were used to update carrier densities. (vi) A simple external circuit in terms of a 50 Ohm series resistance was incorporated in the model. (vii) The model took account of the internal displacement current. (viii) Bulk impact ionization, and contact injection due to thermionic emission and the electron tunneling processes were taken into account. The thermionic emission model used an effective Richardson coefficient of $80 \text{ A/cm}^2/\text{K}^2$. The tunneling currents were calculated based on the Wentzel-Kramers-Brillouin (WKB) approximation within the effective mass theory. (ix) Temperature variations within the device were taken into account by solving the steady-state heat flow equation based on the diffusive Fick's law. A temperature dependent thermal conductivity was used for a more realistic model. Thus: $k(T) = 4.517 \times 10^5 T^{-1.29} \text{ Wm}^{-1}\text{K}^{-1}$ was chosen in keeping with recent experimental reports [8]. (x) The simulation scheme coupled the electrical transport and thermal heating aspects. Such an electro-thermal model was devised by using the power dissipation density predictions of the drift-diffusion transport model as input to the steady-state heat flow equation. (x) The temperatures were computed self-consistently by iterating between the drift-diffusion model (which yields the power generation through current flow distribution), and the thermal solver based on the given power dissipation, until convergence was reached. In this coupled process, changes in the parameters of the transport model due to temperature variations were included for each grid point.

RESULTS AND DISCUSSION

A. One-Dimensional Calculations: Numerical simulations were initially carried out for a one-

dimensional (1D) geometry. The 1D simulations are computationally less intensive, and were meant to serve as a quick check of the overall implementation and for indications of the electrical trends. The following two scenarios were examined: (i) P-N diode with uniform doping on either side and no internal traps or defects. Internal device heating was included. (ii) The uniform diode with electron traps distributed uniformly throughout the device with internal heating.

Scenario I

A discussion of scenario I with no traps but internal heating taken into account is presented first. The internal carrier densities and electric field distributions are Fig. 1(a)-1(c). The depletion region around $1\ \mu\text{m}$ can easily be seen. As expected the electric field profile has a peak at $1\ \mu\text{m}$. However, unlike the predictions of the usual depletion approximation, the electric field does not go to zero at the two ends. A finite, non-zero electric field is maintained to facilitate the carrier drift for maintaining current continuity. Also, the value of the field in the P-region (on the left) is higher than that within the N-region on the right. This is associated with the higher electron mobility that does not require as high an electric field to provide a comparable drift velocity as on the P-side. The peak value occurs at the depletion edge, and is roughly around $2.7 \times 10^6\ \text{V/m}$. The temperature at this relatively low reverse bias is almost unperturbed and has the 300 K ambient value. Figs. 2(a) shows the carrier density distributions at 80 volts reverse bias. The expansion of the depletion region is apparent. The corresponding electric field of Fig. 2(b) has a shape similar to that of Fig. 1(b). However, the peak value is higher at $6.6 \times 10^7\ \text{V/m}$. The internal profiles at 180 Volts are shown in Figs. 3(a)-3(d). The depletion region of Fig. 3(a) is seen to have widened even more. The shape of the electric field distribution of Fig. 3(b) is roughly unchanged (except for a positive slope at the left end). The peak value is quite high at $1.25 \times 10^8\ \text{V/m}$. The corresponding power dissipation associated with the conduction current is shown in Fig. 3(c). The peak occurs on the P-side close to the negatively biased left end that is the source for electron injection. The depletion region, on the other hand, has the least supply of free carriers. Hence, despite the large electric field, the Joule heating due to charge conduction is small. The corresponding steady-state temperature profile is shown in Fig. 3(d). It roughly follows the power dissipation profile. Though there is non-uniformity, the peak deviation is less than a degree. Hence, almost negligible device heating is predicted. Finally, the situation at a bias of 235 Volts is discussed. The carrier profiles are shown in Fig. 4(a). Unlike Fig. 3(a), the depletion region is shorter. This is the direct consequence of internal impact ionization, and the generation of electron-hole pairs. For a similar reason, the density of holes within the P-side on the left has a rectangular shape, instead of the triangular profile of Fig. 3(a). On the N-side too, the generation produces a slight slope in the electron profile. Fig. 4(b) shows the power

dissipation profile. The minimum occurs over the depletion region for the reason already state above. However, the temperature profile of Fig. 4(c) has a maxima towards the central part of the device. Since the two boundaries are assumed to be at the ambient temperature, the peak temperature rise is roughly at the midway point. A maximum temperature of 540 Kelvin is predicted, and is considerably higher than the 300 K ambient.

Scenario II

Internal traps were included next to probe their role on the device characteristics. The presence of screw dislocation lines running parallel to the device axis (i.e. perpendicular to the p-n junction plane) is known to give rise to electron trapping sites. Hence, the inclusion of electron traps was meant to model the presence of a dislocation line running through the device from the P-side to the N-region. The density was chosen to be $5 \times 10^{16} \text{ cm}^{-3}$ with an electron capture cross-section of $5 \times 10^{-14} \text{ cm}^2$. Simulation results of the carrier profiles for a 80 volt reverse bias are shown in Fig. 5(a). Two differences are apparent between the curves of Fig. 2(a) and Fig. 5(a). First, the density of electrons is much smaller. This is the result of trapping at the sites. Next, the depletion region is somewhat smaller. This is due to the availability of electrons within this region due to their release from the trap sites. This mechanism provides a supply of carriers for possible impact ionization and avalanche action. The internal temperature profile of Fig. 5(b) shows a near-symmetric curve with a maximum of 342 Kelvin. This value was higher than the previous case, and again is the result of higher internal currents leading to greater Joule dissipation. The results for 180 volts for scenario II are shown in Figs. 6(a)-6(b). The electron profile of Fig. 6(a), as compared to the corresponding Fig. 3(a) of scenario I, is lower due to the presence of trapping sites. Also, the depletion layer is not as wide. The temperature with the electron trap line is much higher. The peak from Fig. 6(b) is at 455 Kelvin. Hence, significant increases in internal heating are predicted for a diode containing traps or dislocation lines.

B. Two-Dimensional Calculations: Numerical simulations were next carried out for a two-dimensional geometry. Transverse symmetry was assumed in the process. Since the existence of potential electron traps in SiC diodes is virtually certain, the $5 \times 10^{16} \text{ cm}^{-3}$ density of single traps was used as with the 1D calculations described above. The electric field profile for a moderately low 80 volt bias is shown in Fig. 7(a). It has almost no features along the transverse direction. Similarly, the electron density shown in Fig. 7(b) is also more or less uniform. However, for a much larger bias of 180 V, the electron density profile of Fig. 8 reveals a distinct inhomogeneity. Two filamentary features are evident, each lying on either side of the defect line taken to be located midway through

the device. These localized increases in electron density can very well produce the current filaments that have been seen experimentally. Finally, at an even higher voltage of 245 V shown in Fig. 9, the filamentary shape is even more pronounced. It is thus, clearly demonstrated through the present numerical calculations that filamentary inhomogeneities can develop naturally in the SiC diodes at high voltages. The prediction is that these will be located close to defect or dislocation lines.

C. I-V Characteristics:

Finally, as part of this study of SiC p-n diodes, the current-voltage characteristics were also probed. Fig. 10 shows the I-V characteristics predicted by the numerical model for the SiC P-N diode under various conditions. When no traps are considered the curve exhibits a negative differential conductance (NDC). As is well known, this is potentially an unstable mode of operation and can lead to current filamentation. In actual practice, some internal point defect or inhomogeneity will be present. This is likely to trigger an instability arising from the NDC. Beyond the NDC region, the current is not predicted to increase with voltage appreciably. Instead, based on Fig. 10, the current would almost reach a saturating limit as the result of strong increases in the internal device temperature. The temperature increases reduce the carrier mobility and drift velocities, and hence, quench transport. The inclusion of internal traps is seen to eliminate the NDC. Thus, the 1D analysis suggests some advantage in having internal defects for improved I-V characteristics. As with the previous case without traps, the current levels for the trap scenario reduce as well. This again, is due to the reductions in the transport parameters.

Table I. Parameters Used in the Numerical I-V Simulations Of the SiC Diode

PARAMETER	VALUE (UNITS)
μ_n^{\min}	20 cm ² /Vs
μ_p^{\min}	5 cm ² /Vs
μ_n^{delta}	380 cm ² /Vs
μ_p^{delta}	70 cm ² /Vs
N_n^{μ}	4.5×10^{17} cm ⁻³
N_p^{μ}	1×10^{19} cm ⁻³
$\gamma(n)$	0.45
$\gamma(p)$	0.5
α_n	-3
α_p	-3
β_n	2
β_p	2
v_n^{sat}	2×10^7 cm/s
v_p^{sat}	2×10^7 cm/s
b_n	1.273×10^7 V/cm
b_p	1.4×10^7 V/cm
Electron & Hole Effective Masses	$(0.07 \text{ \& } 0.47) * 9.1 \times 10^{-31}$ Kg
Trap Density	5×10^{16} cm ⁻³
Trap Energy From Conduction Band	1.5 eV
Electron Trapping Cross Section	5×10^{-14} cm ²
Donor & Acceptor Densities	$10^{17} \text{ \& } 10^{18}$ cm ⁻³
Donor Energy (from conduction band)	0.075 eV
Acceptor Energy (from valance band)	0.2 eV

REFERENCES

1. P. G. Neudeck, W. Huang, and M. Dudley, IEEE Trans. Electron Devices **46**, 478 (1999).
2. M. Ruff, H. Mitlehner, and R. Helbig, IEEE Trans. Electr. Dev. **41**, 1040 (1994).
3. M. Bhatnagar and B. J. Baliga, IEEE Trans. Elec. Dev. **40**, 645 (1993).
4. H. Morkoc, S. Strite, G. B. Gao, M. E. Lin, B. Sverdlov, and M. Burns, J. Appl. Phys. **76**, 1363 (1994).
5. For example, O. Madelung, in Physics of Group IV Elements and III-V Compounds, Group III, Vols. 17a and 22a, Landolt-Bornstein New Series (Springer-Verlag, Berlin, 1981).
6. W. Shockley, Solid State Electr. **2**, 36 (1961).
7. R. Raghunathan and B. J. Baliga, Solid State Electr. **43**, 199 (1999).
8. St. Muller, R. Eckstein, J. Fricke, D. Hofmann, R. Hofmann, R. Horn, H. Mehling, and O. Nilsson, in Materials Science Forum **264-268**, 623 (1998).
9. J. L. Moll, Proc. IRE **46**, 1076 (1958).
10. P. Mark and M. A. Lampert, *Current Injection in Solids*, (Academic Press, New York, 1970.)

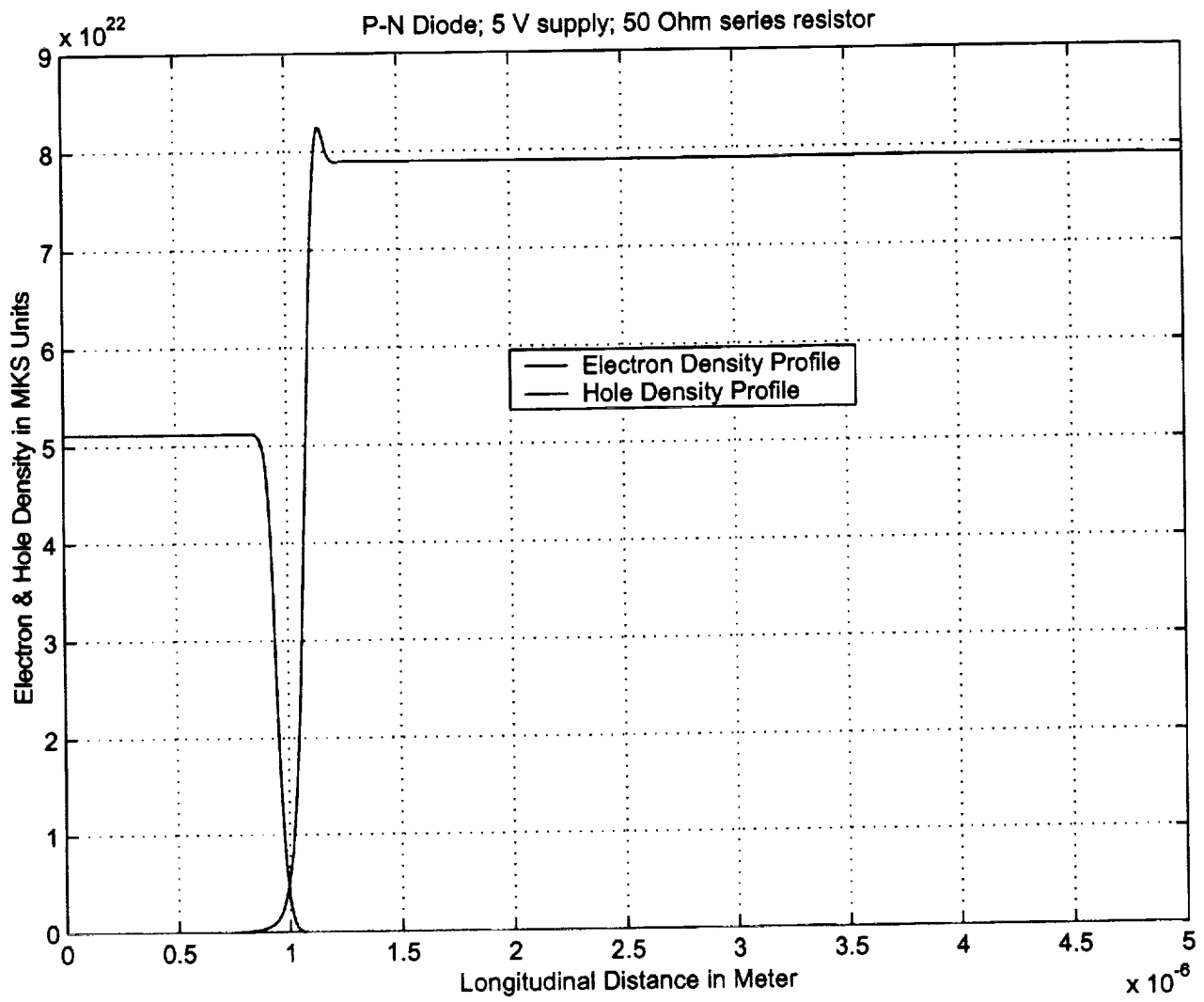


Figure 1(a)

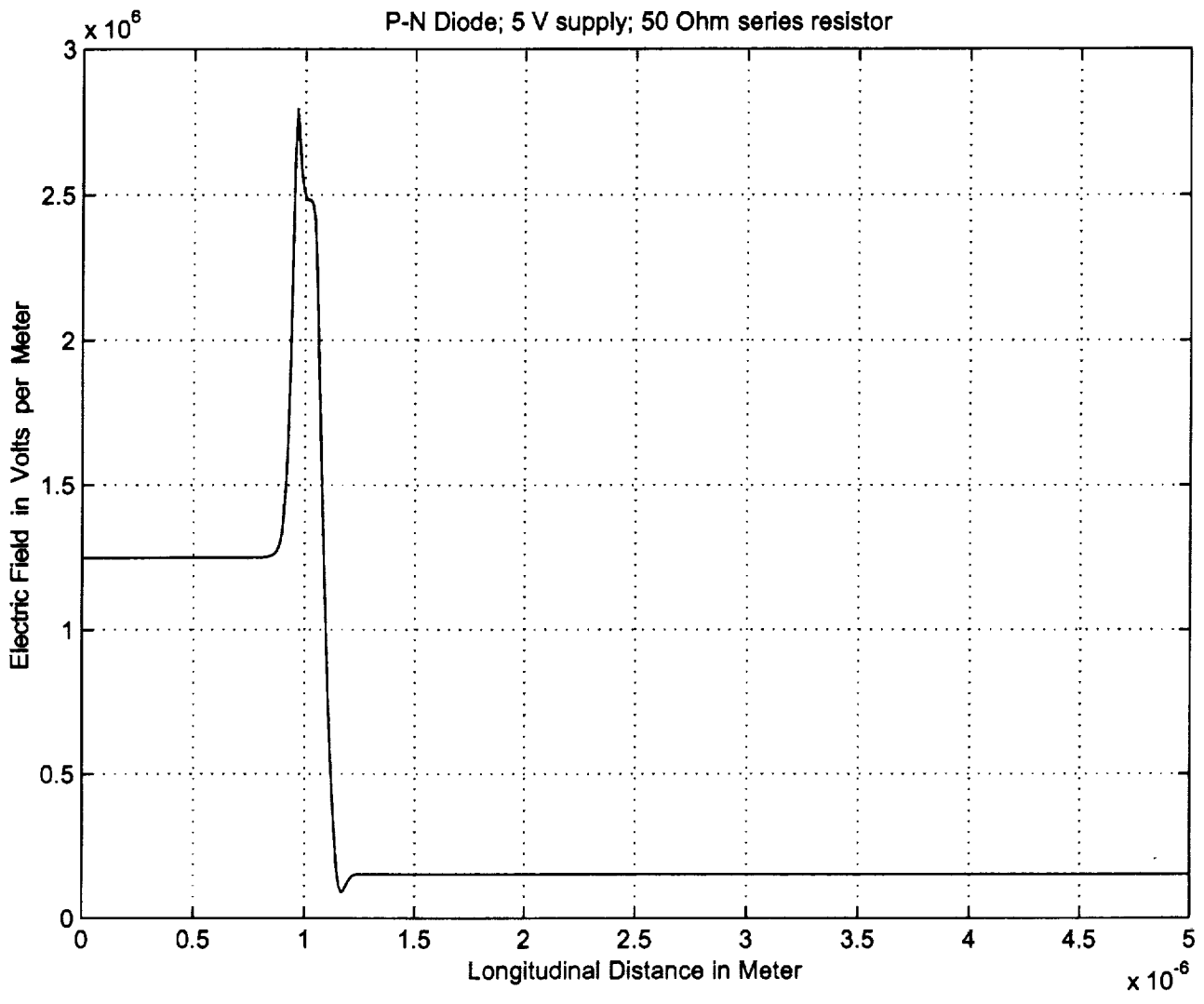


Figure 1(b)

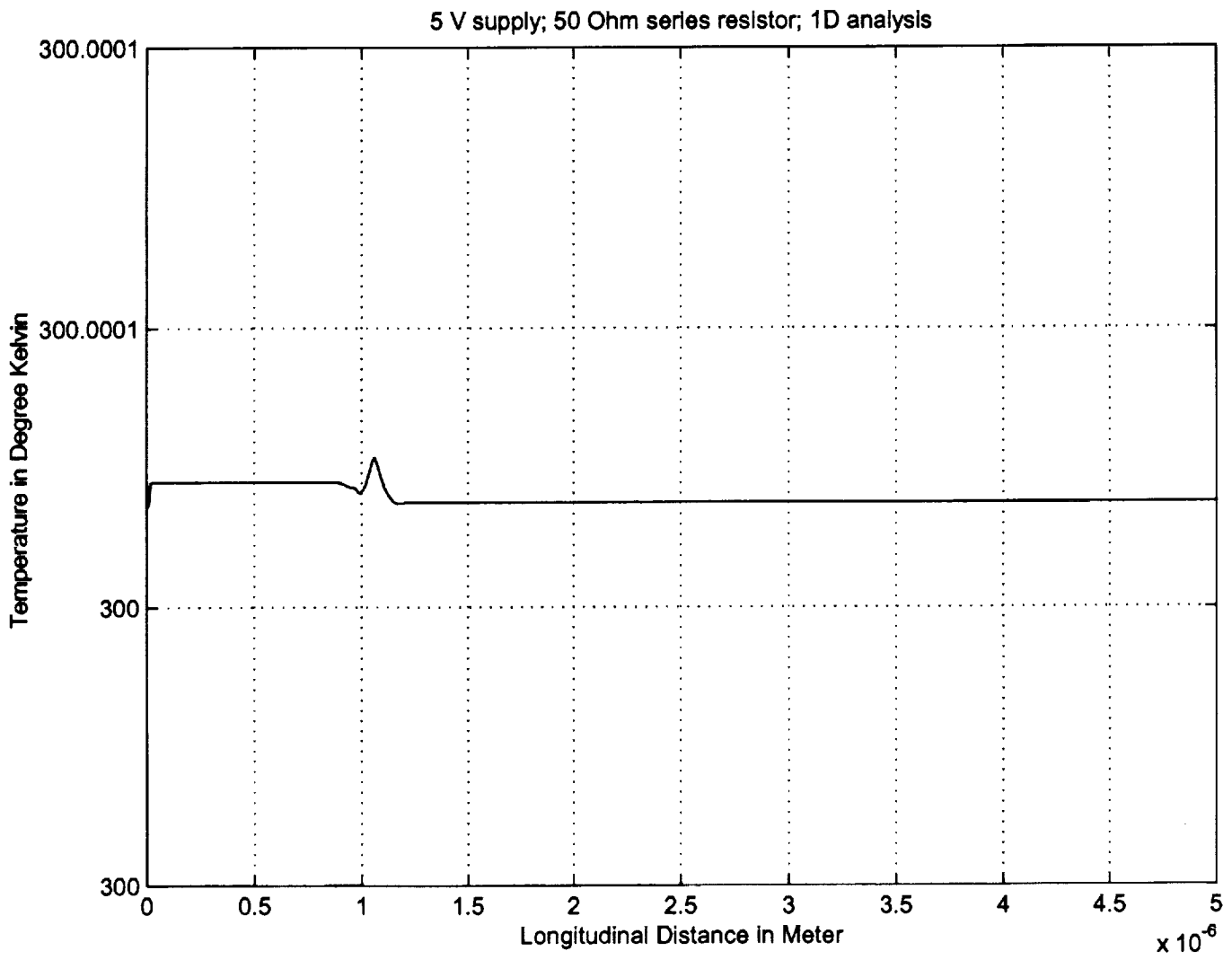


Figure 1(c)

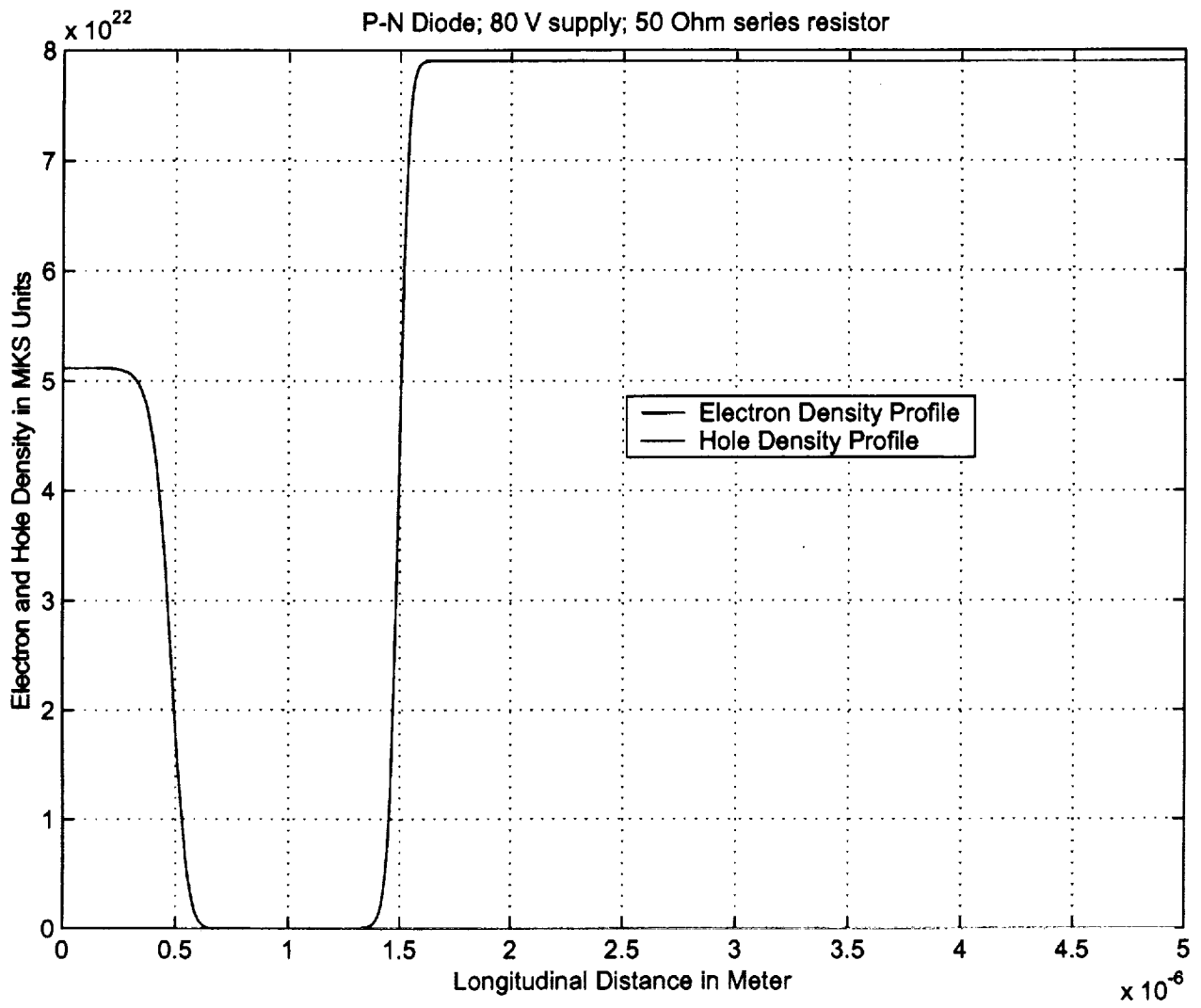


Figure 2(a)

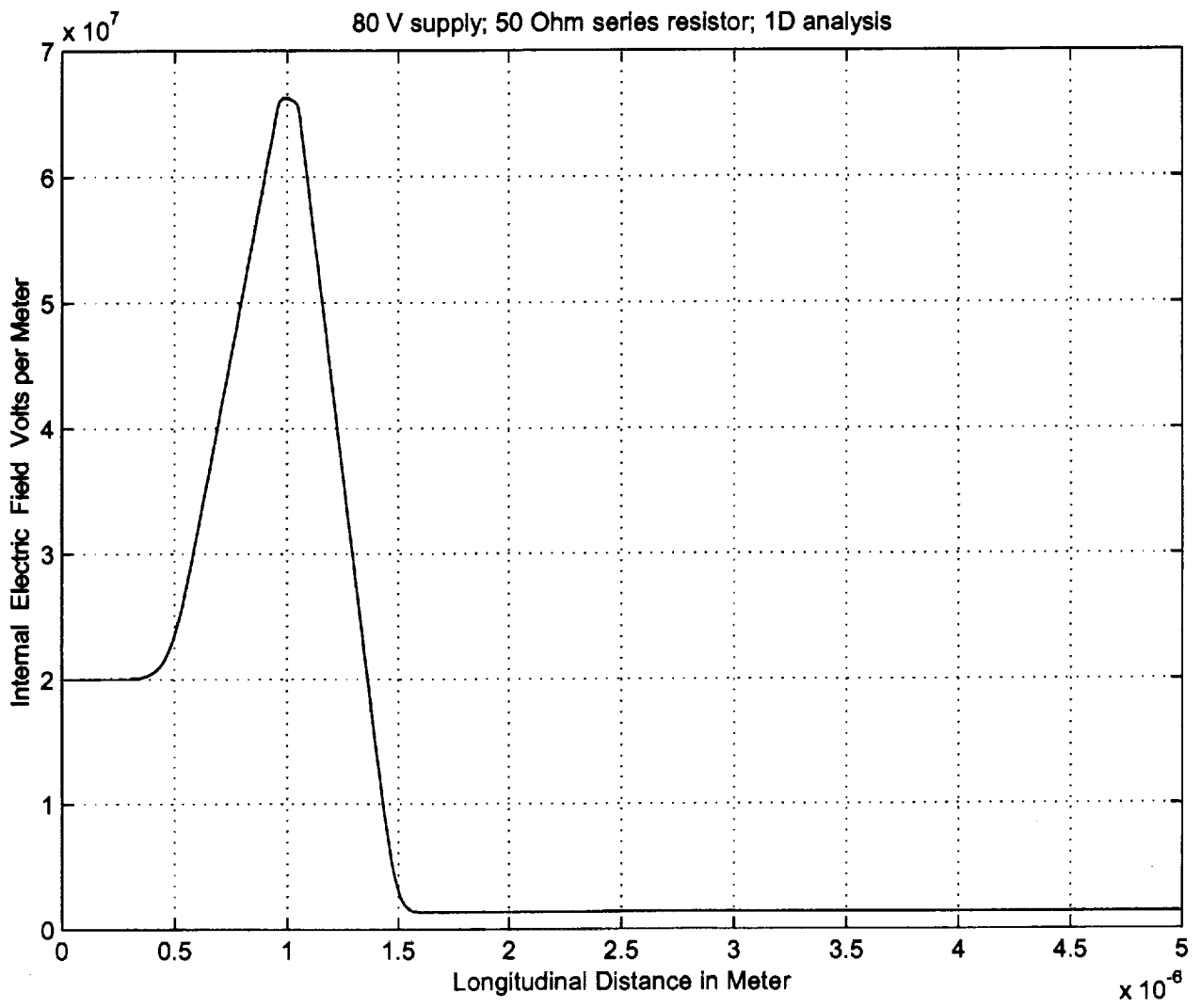


Figure 2(b)

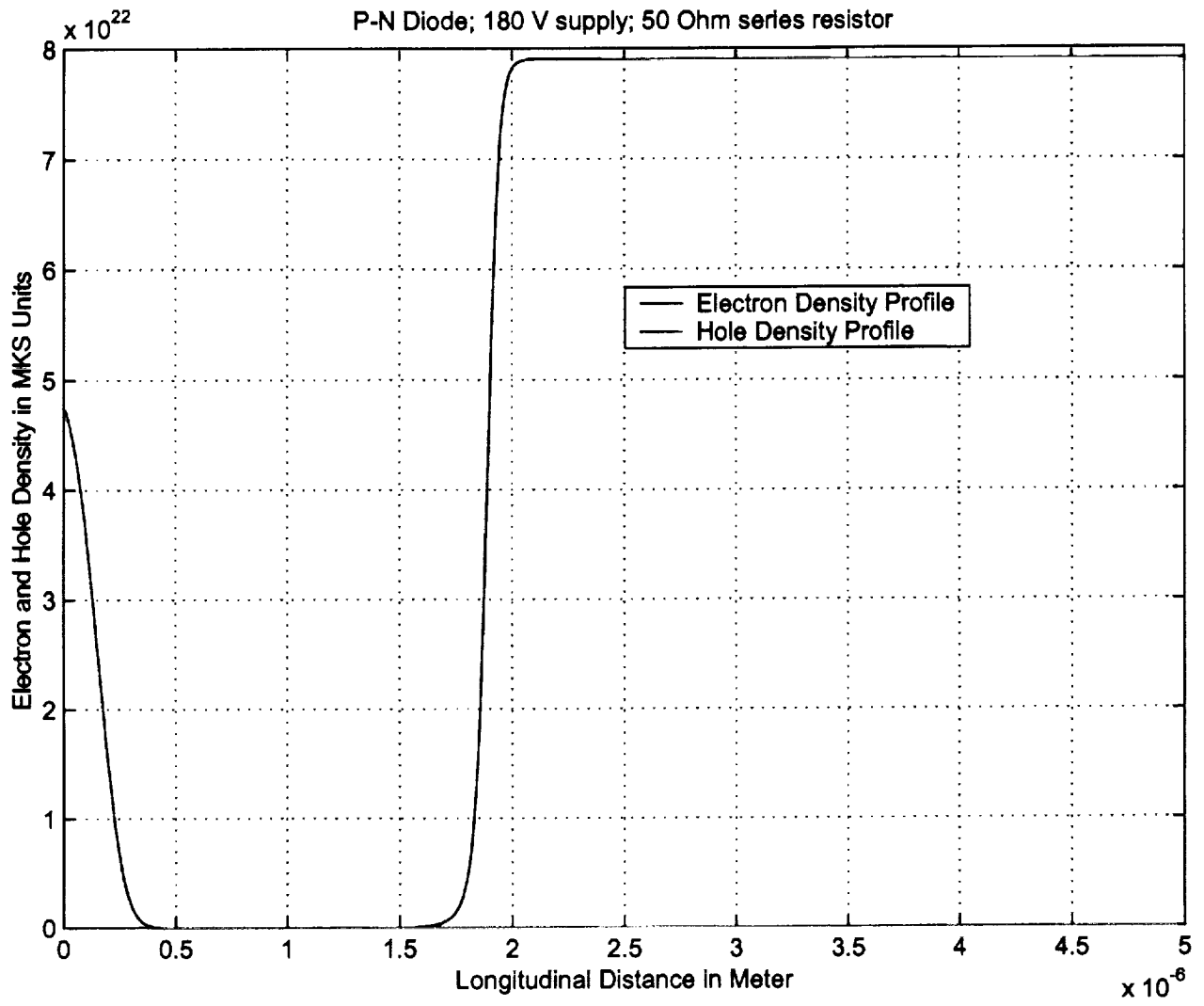


Figure 3(a)

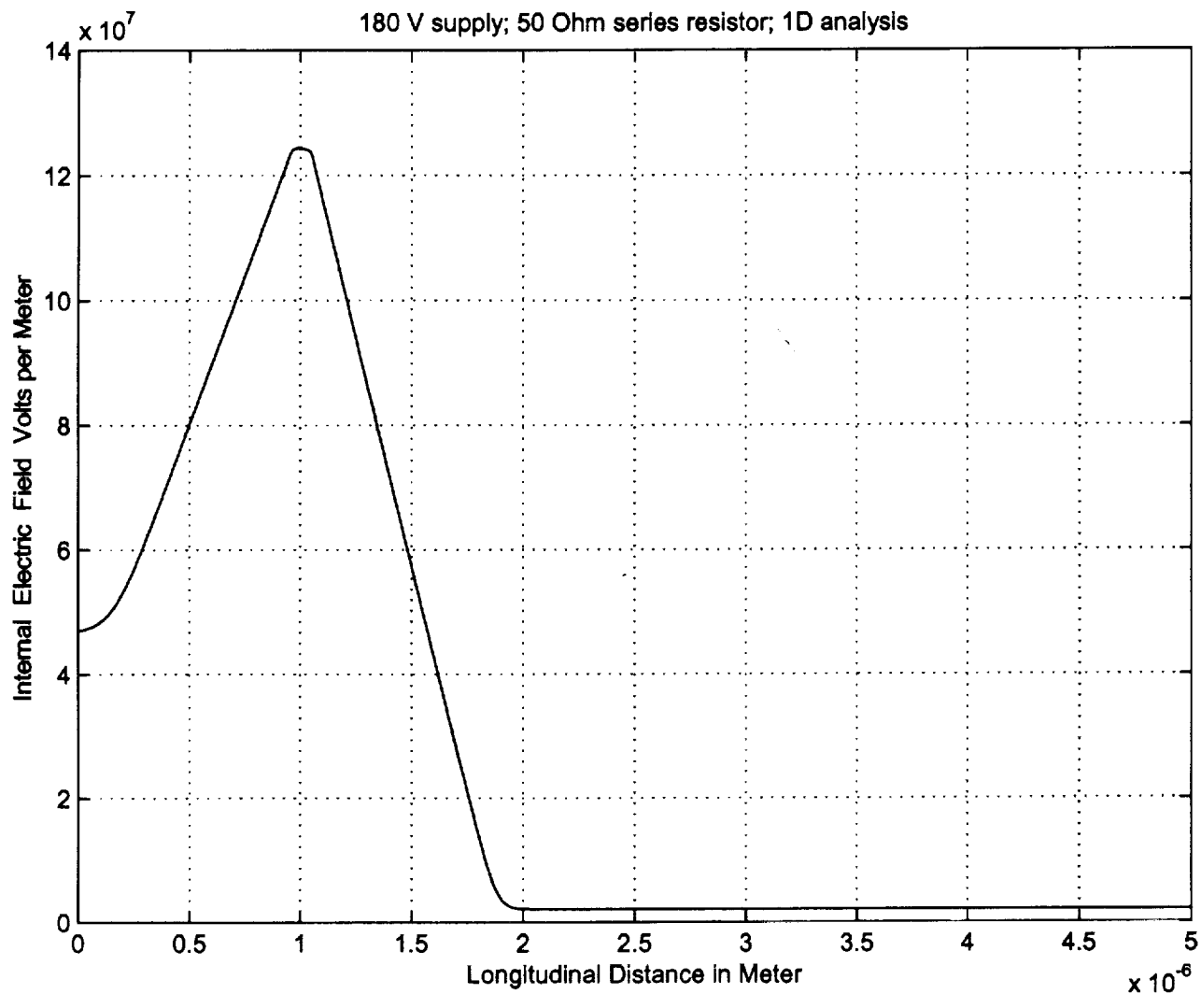


Figure 3(b)

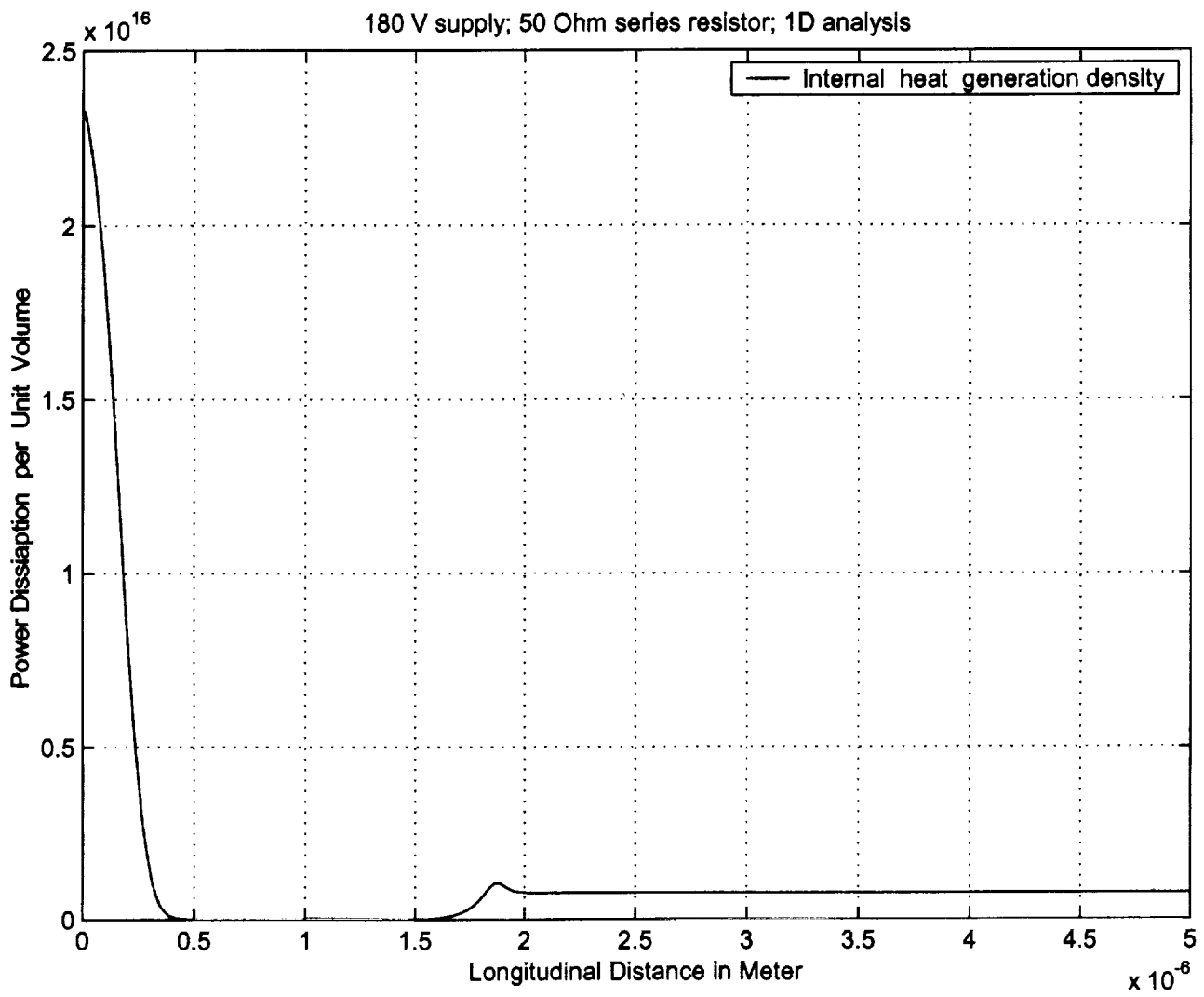


Figure 3(c)

180 V supply; 50 Ohm series resistor; 1D analysis

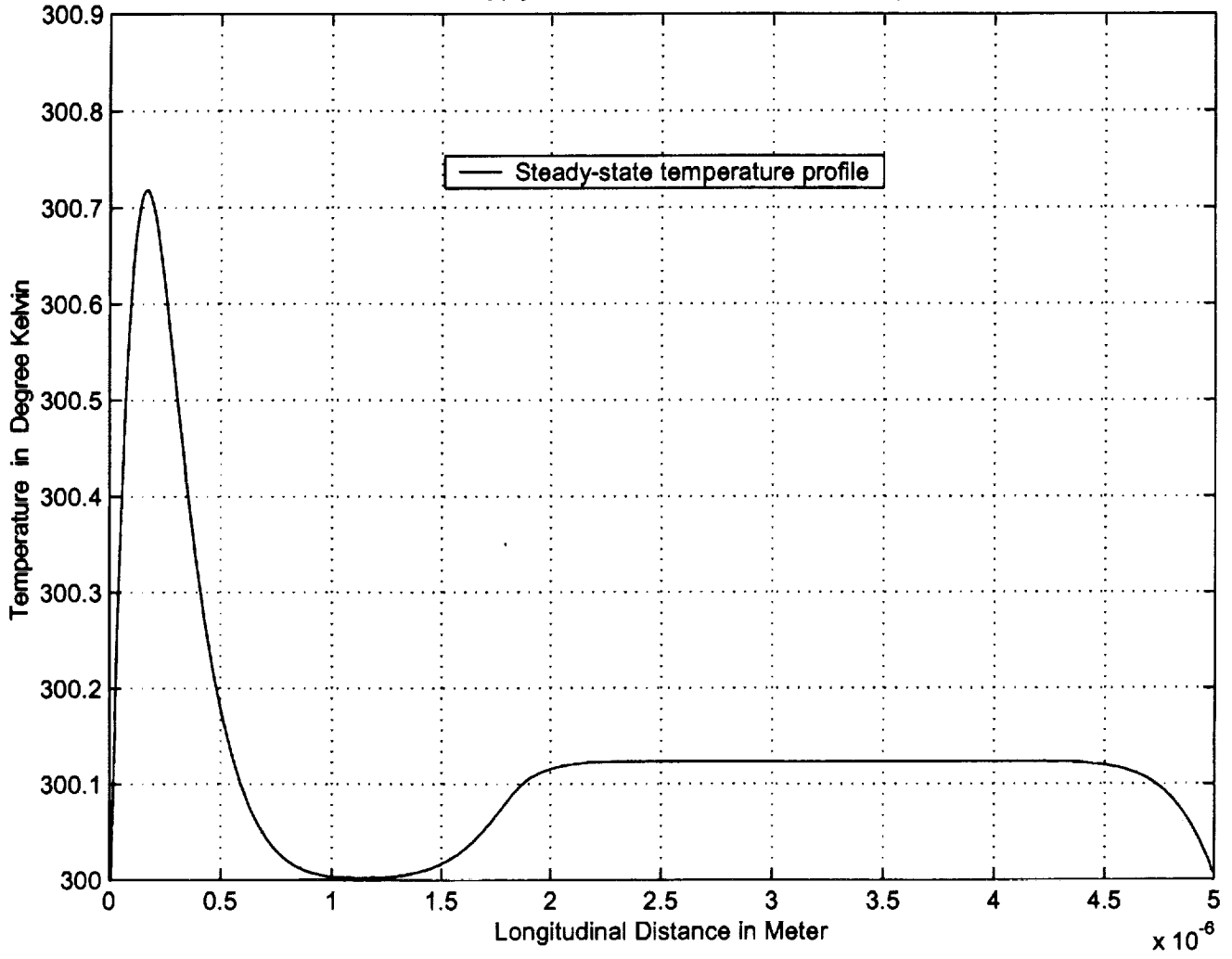


Figure 3(d)

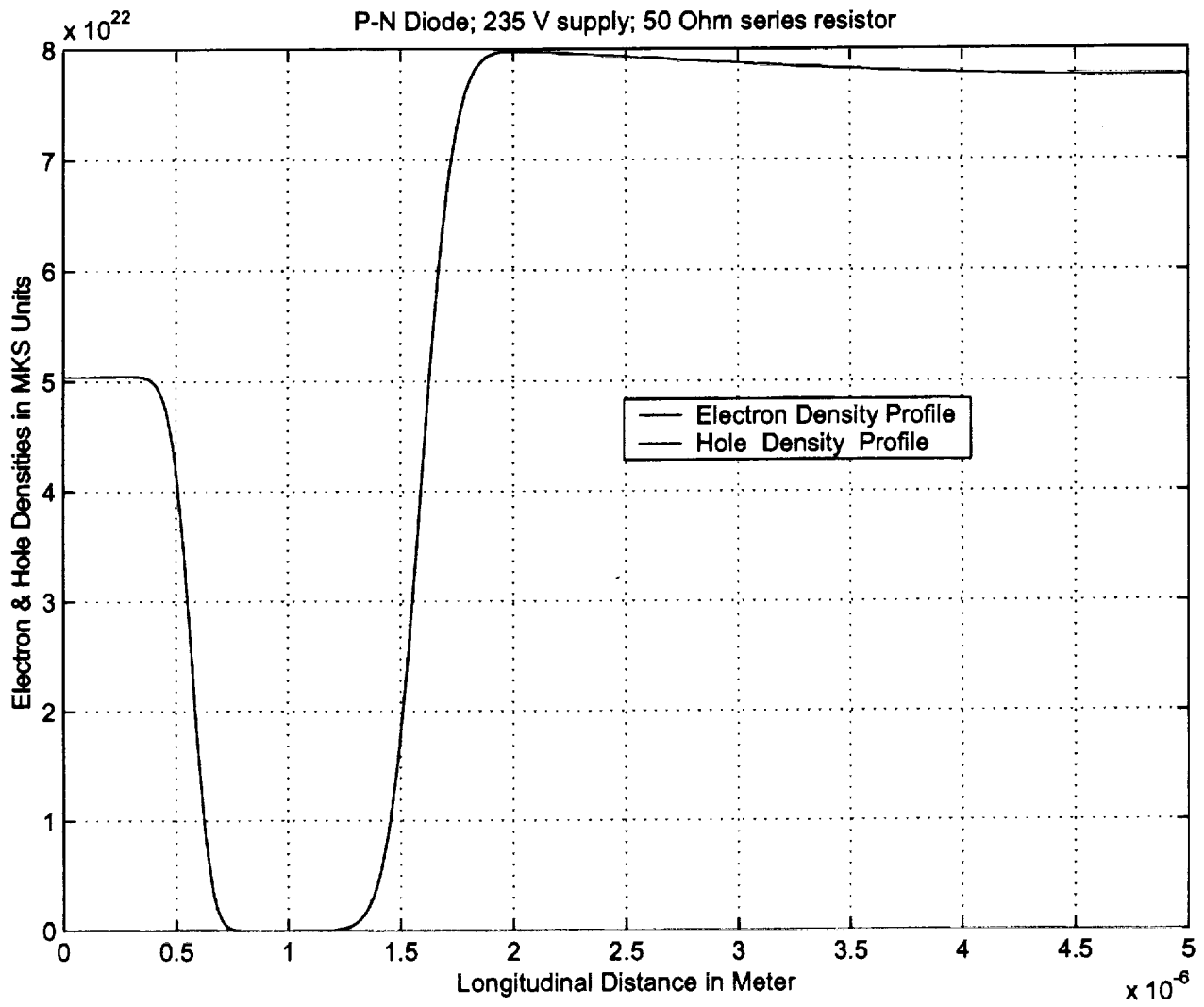


Figure 4(a)

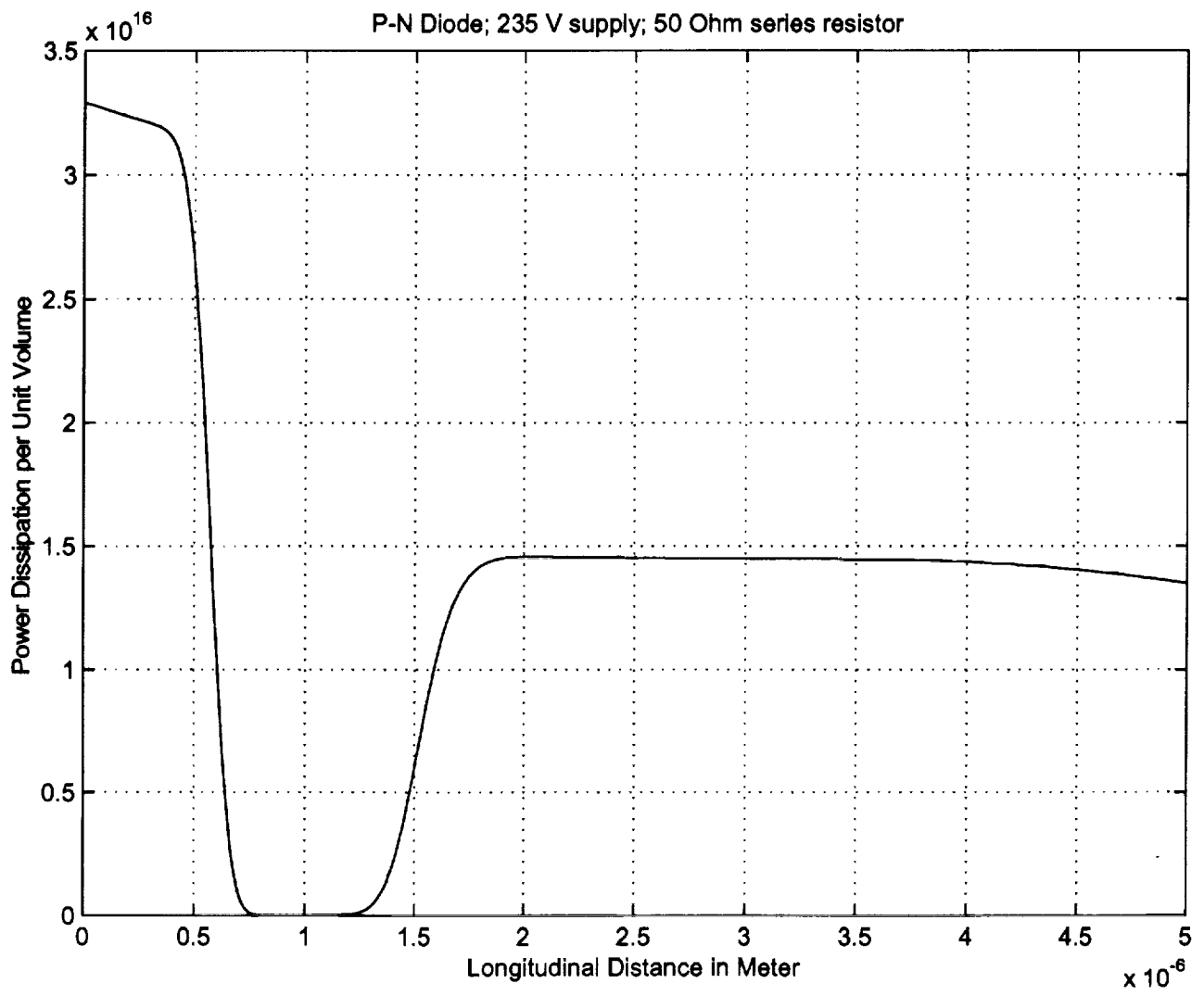


Figure 4(b)

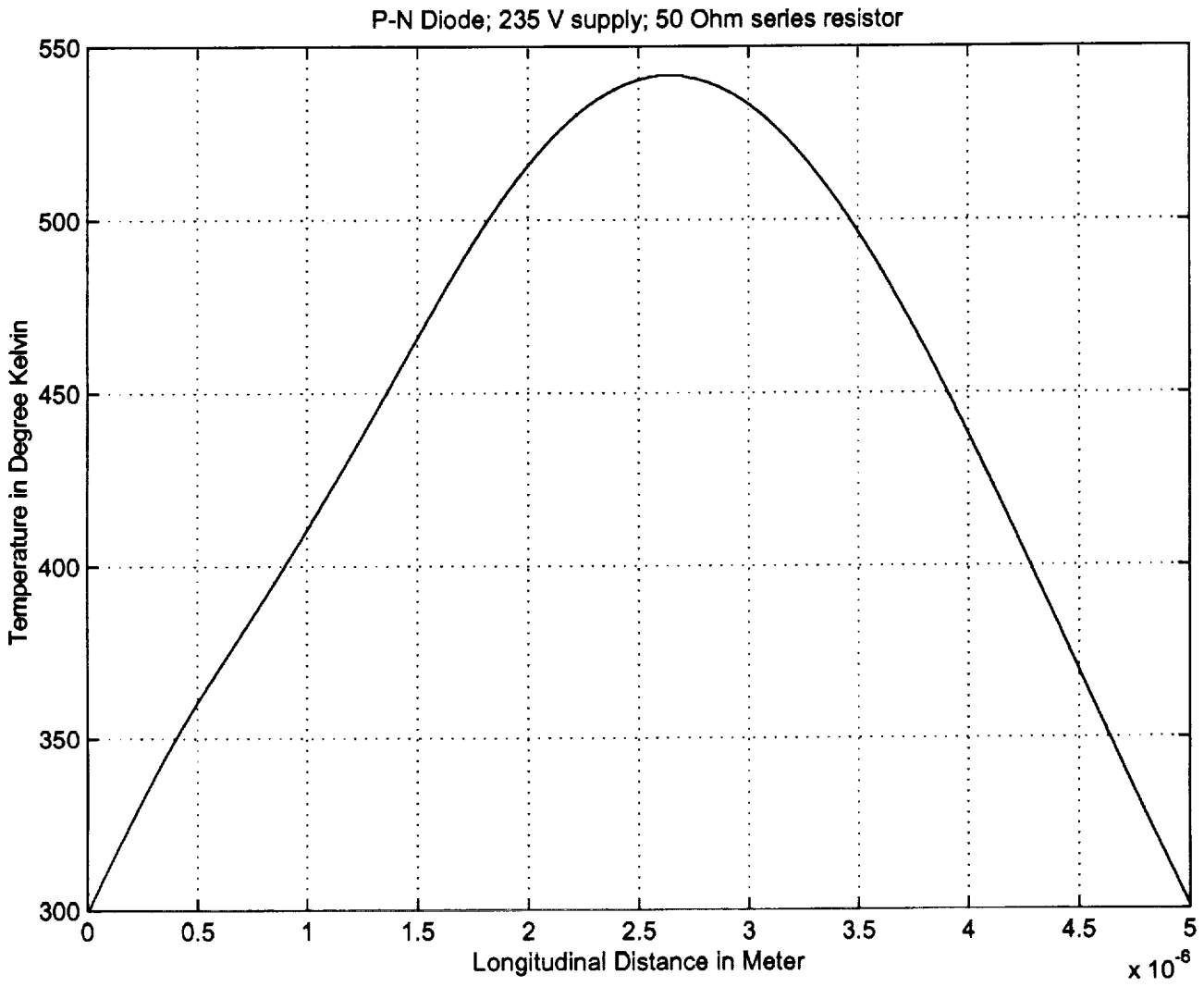


Figure 4(c)

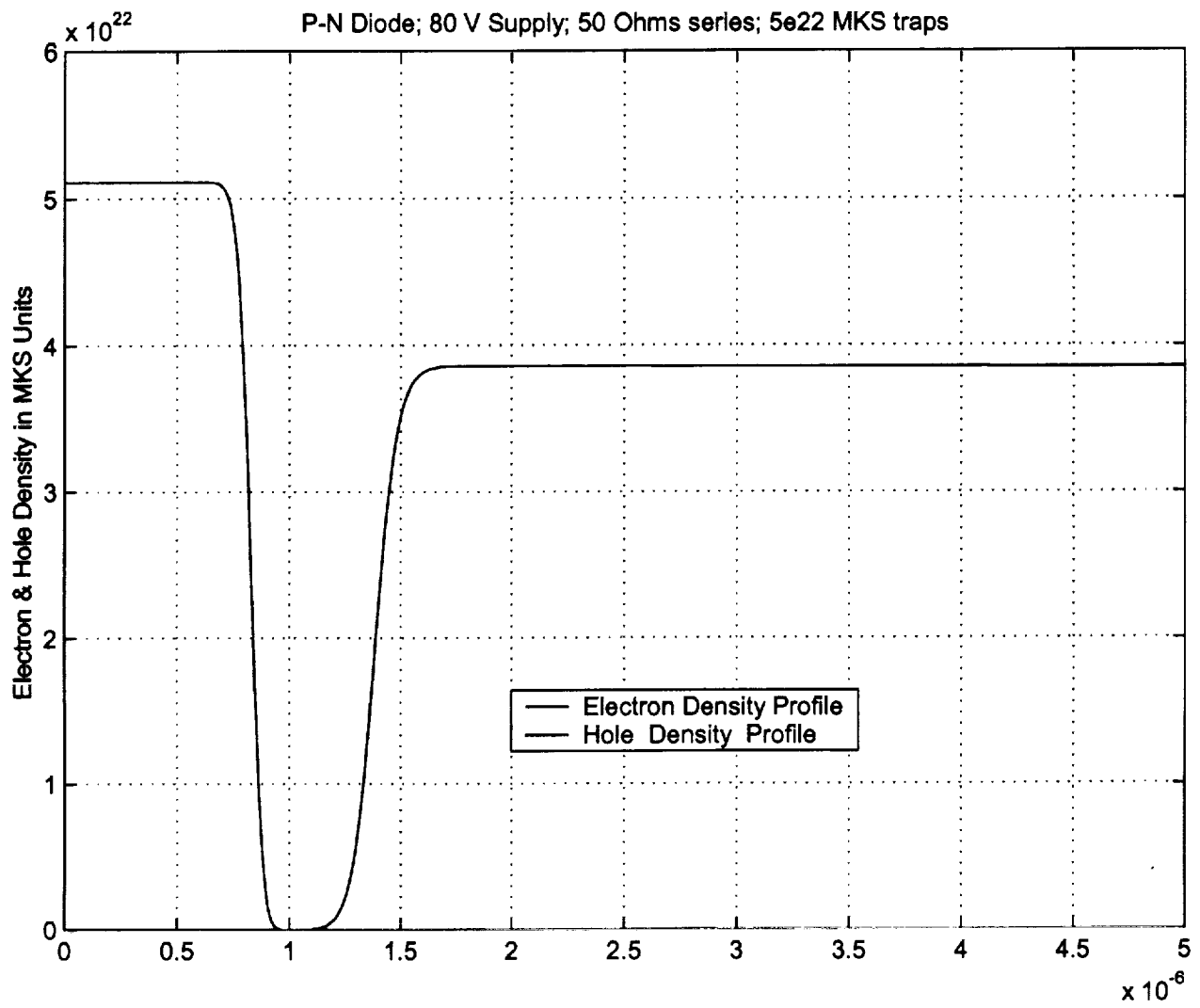


Figure 5(a)

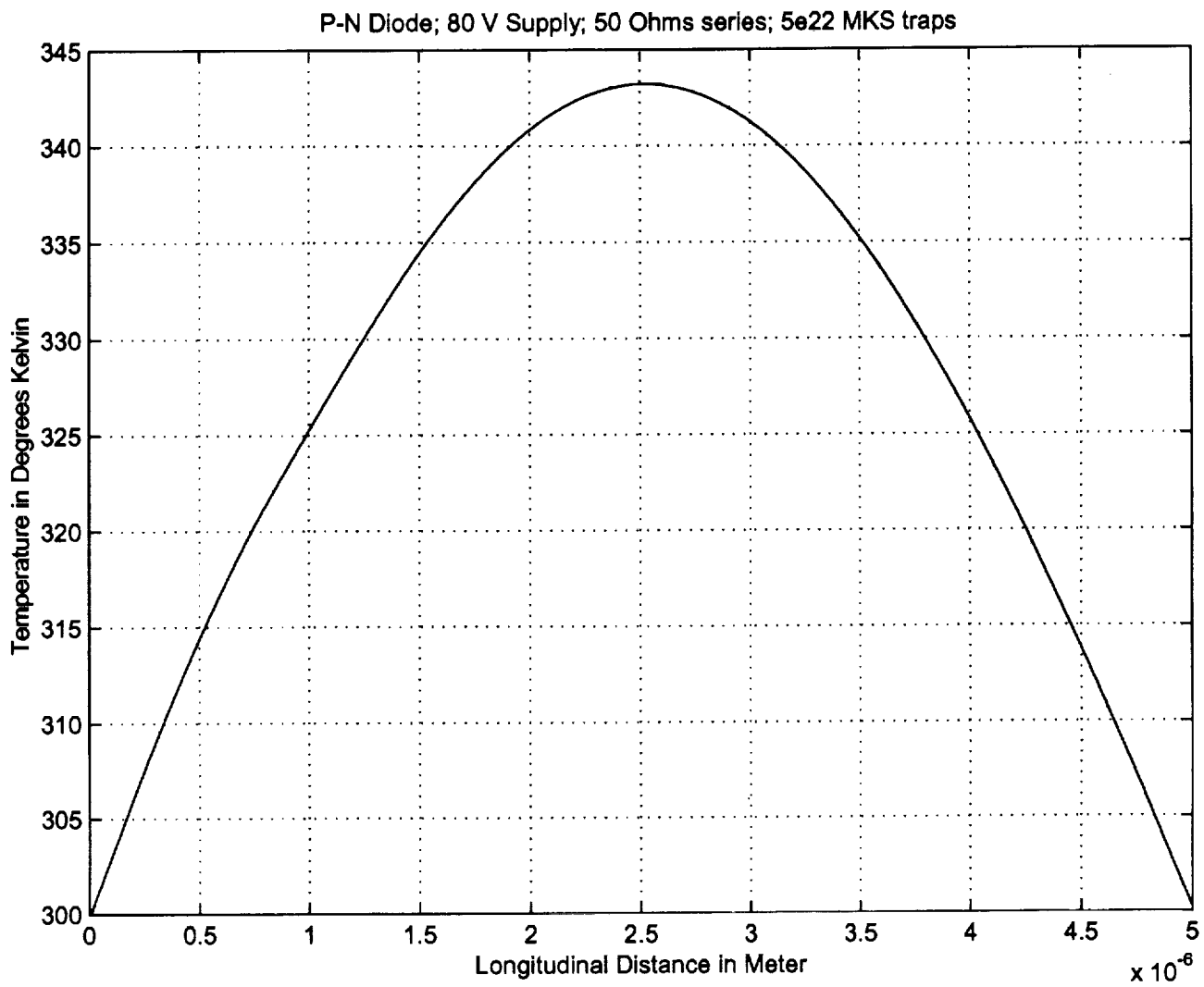


Figure 5(b)

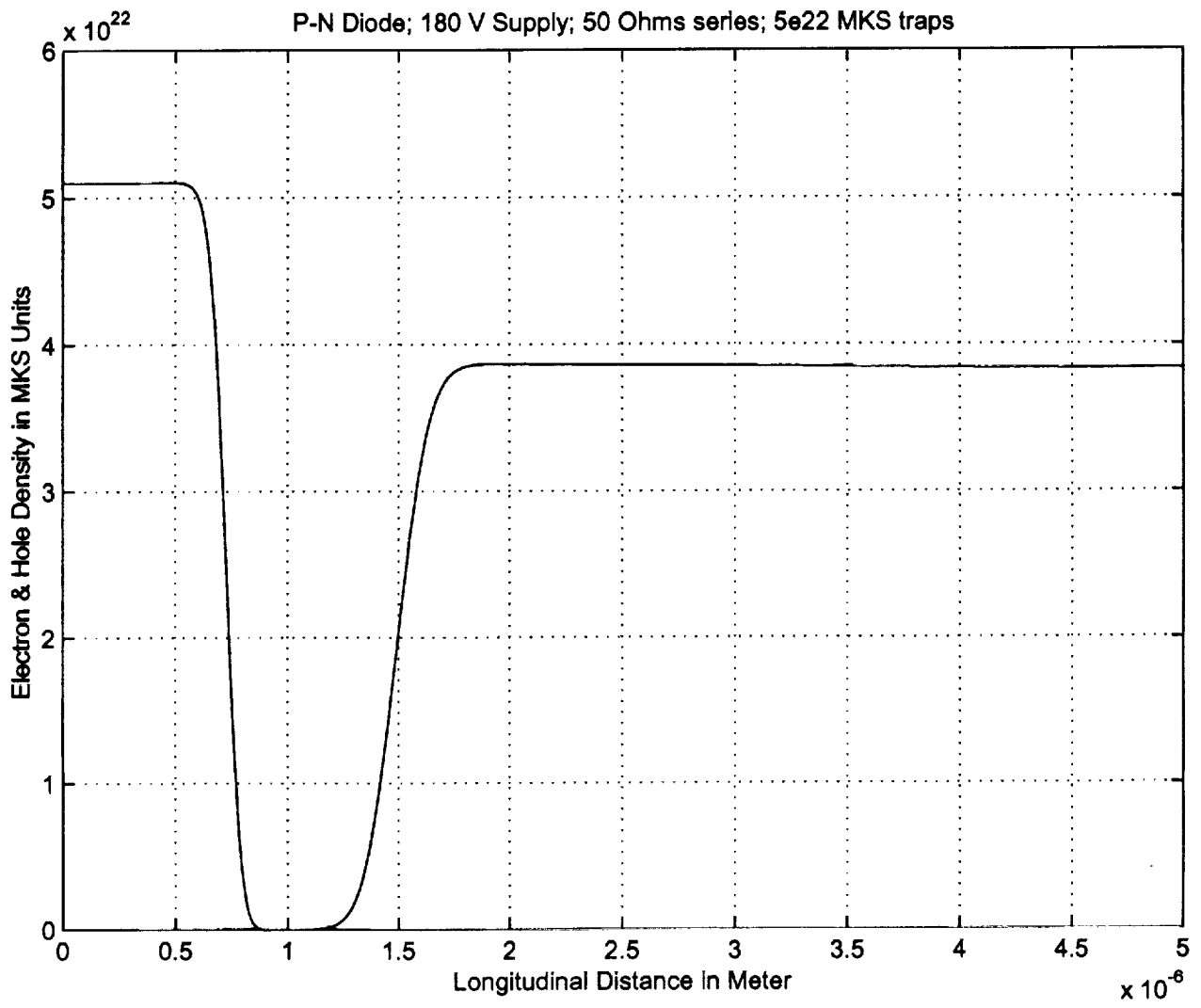


Figure 6(a)

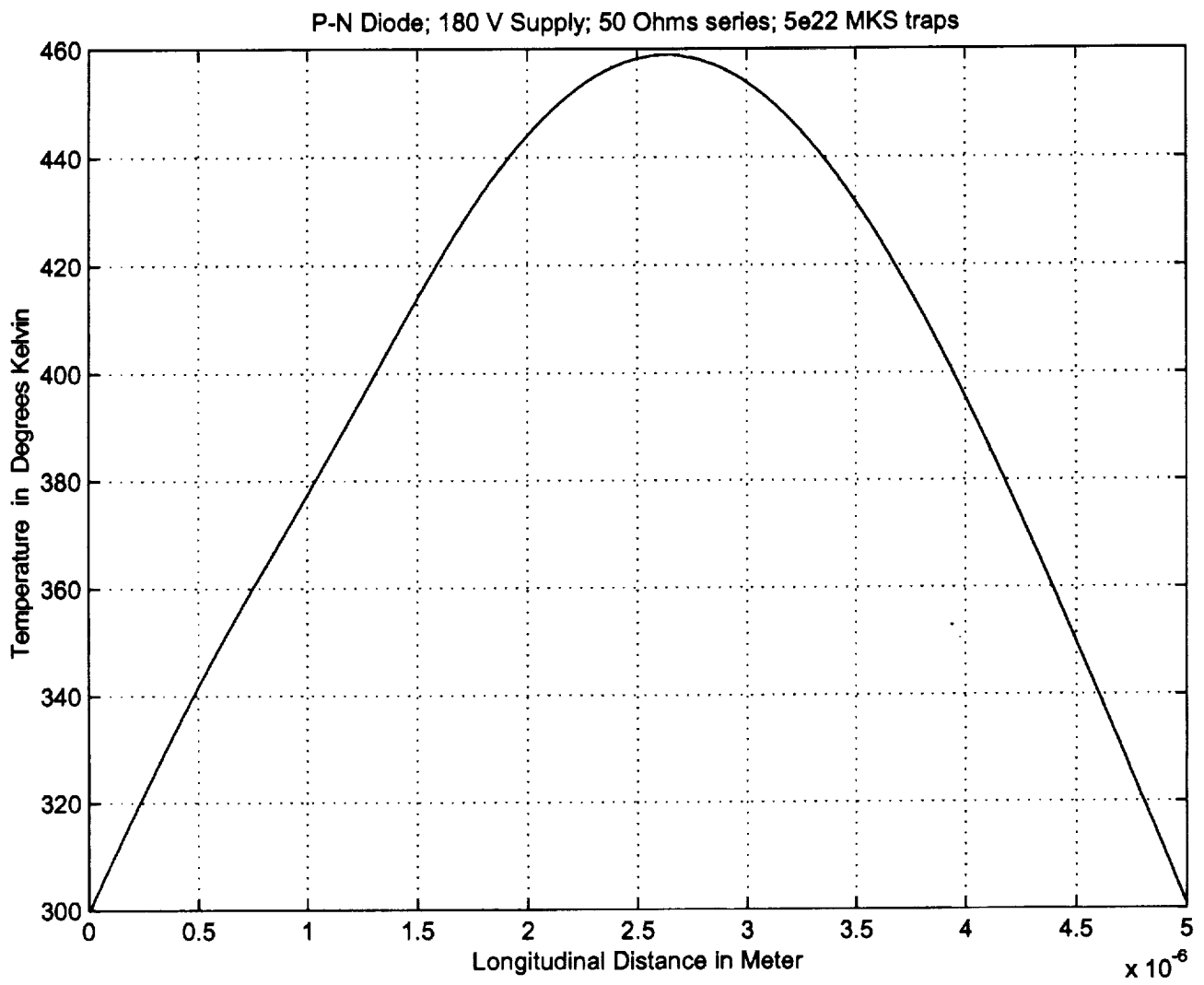


Figure 6(b)

$N_T=5e22$; $E_T=0.9 \cdot E_g$; No Heating; Longitudinal Trap Line Midway; $V_A=80$ V

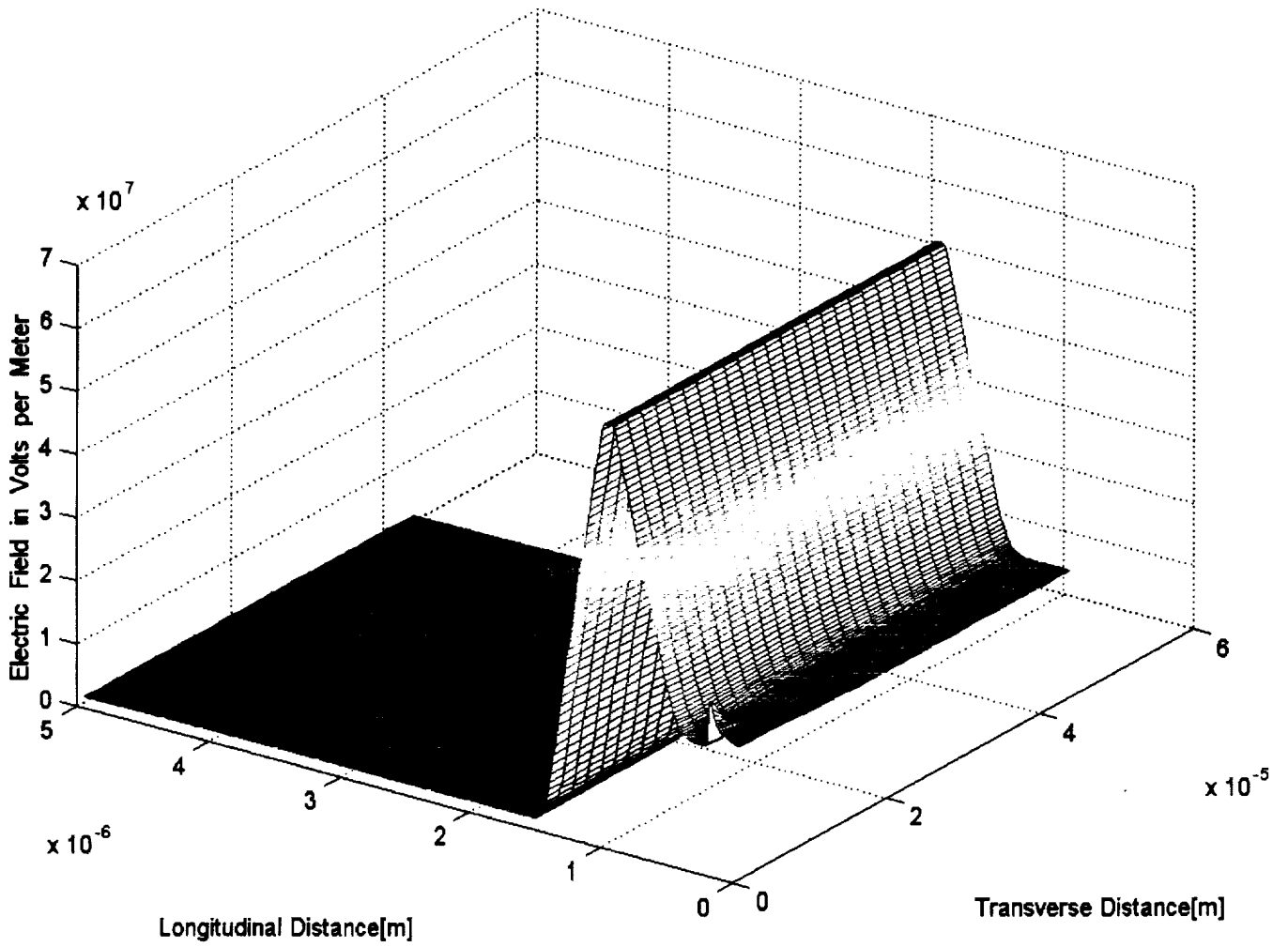


Figure 7(a)

$N_T=5e22$; $E_T=0.9 \cdot E_g$; No Heating; Longitudinal Trap Line Midway; $V_A=80$ V

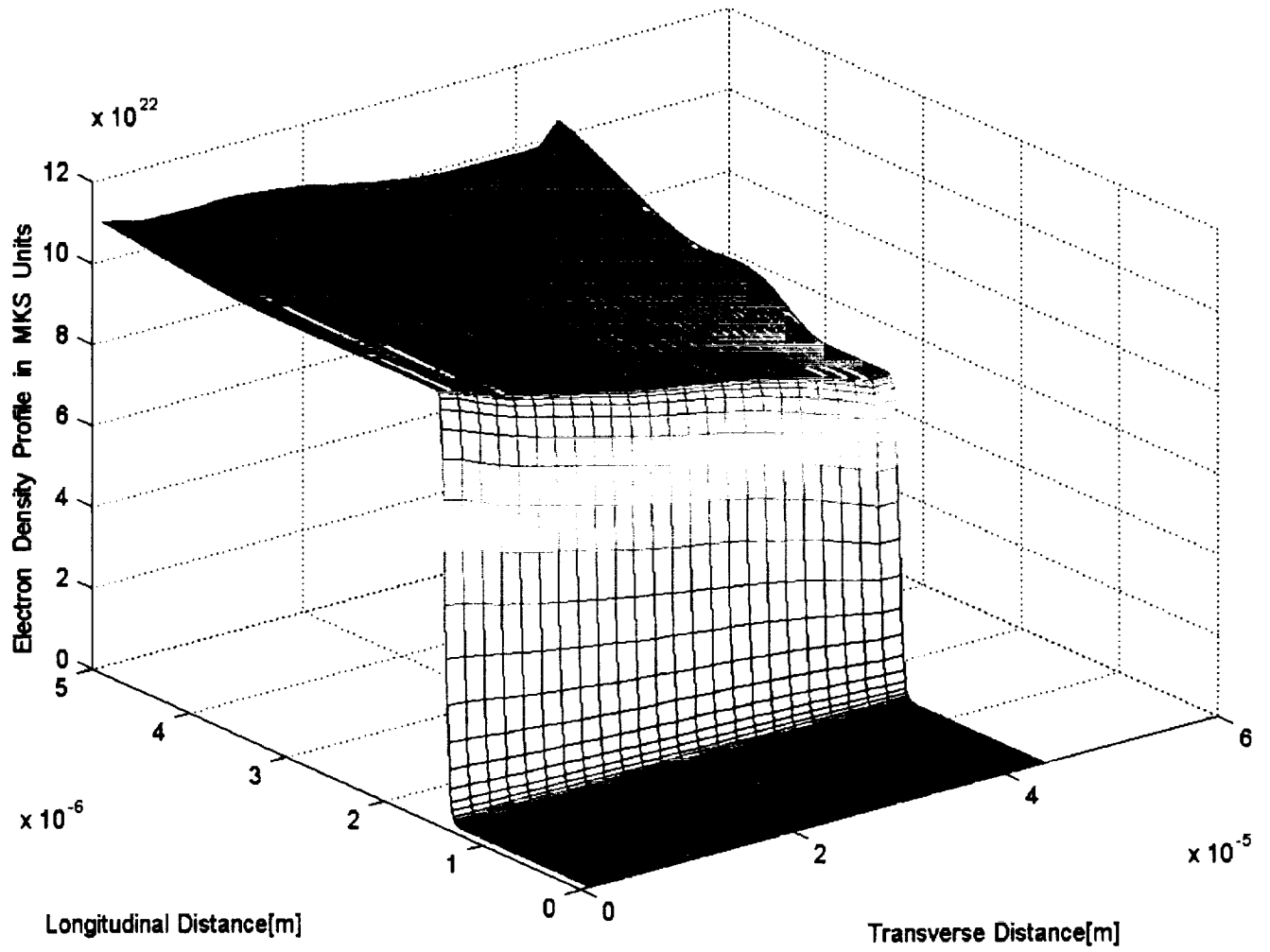


Figure 7(b)

$N_T=5e22$; $E_T=0.9E_g$; No Heating; Longitudinal Trap Line Midway; $V_A=180$ V

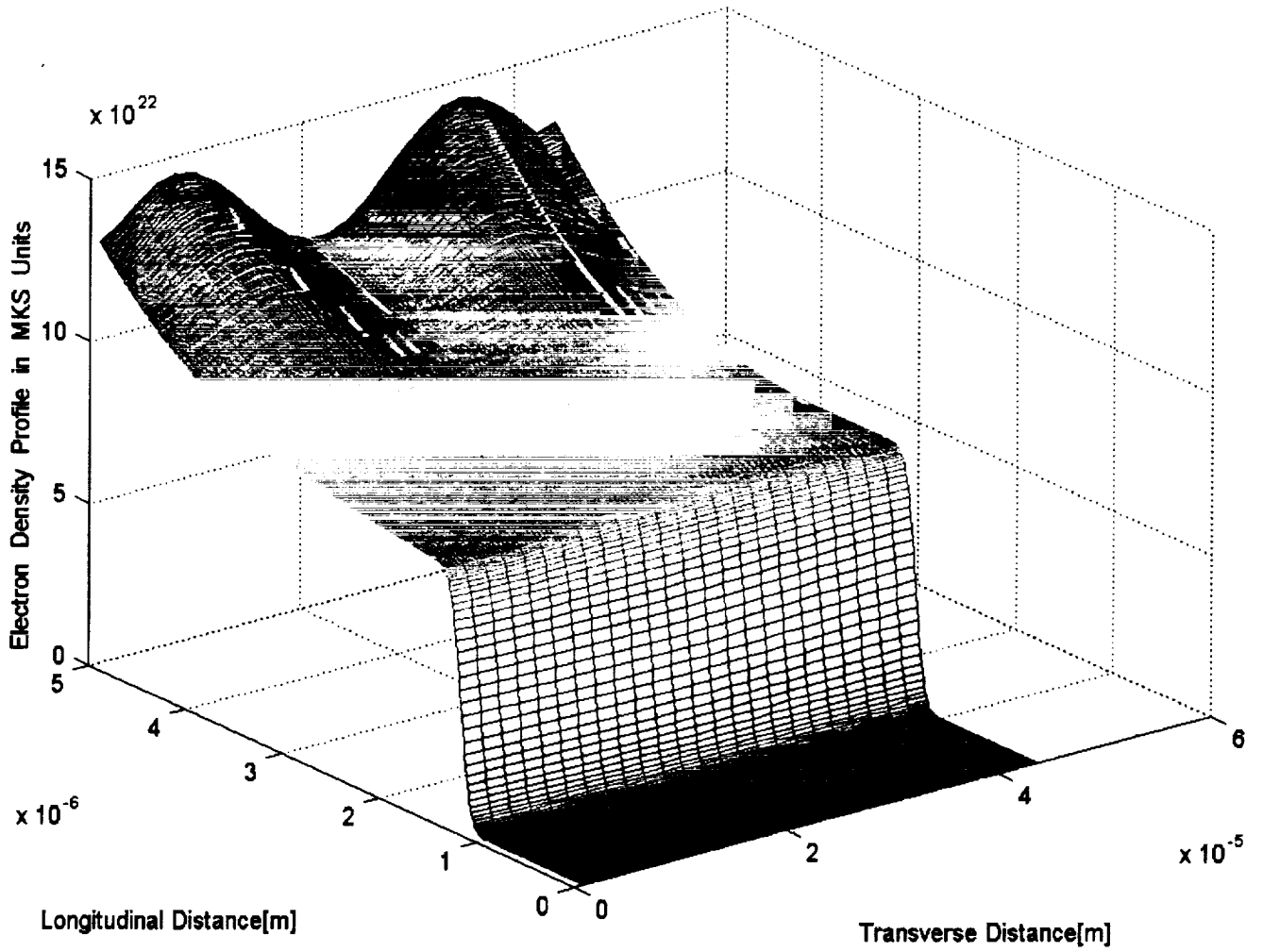


Figure 8

$N_T=5e22$; $E_T=0.9^*E_g$; No Heating; Longitudinal Trap Line Midway; $V_A=245$ V

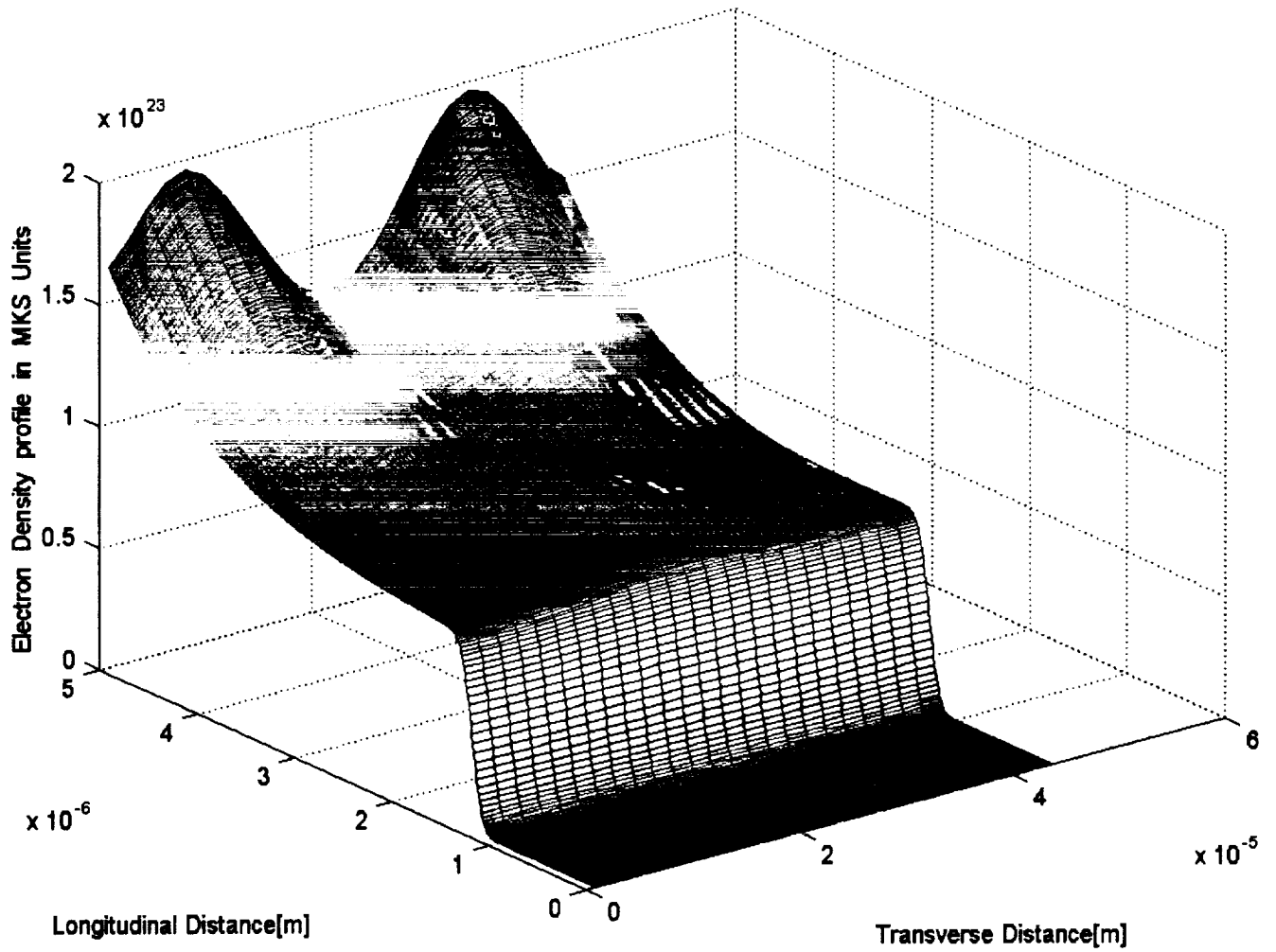


Figure 9

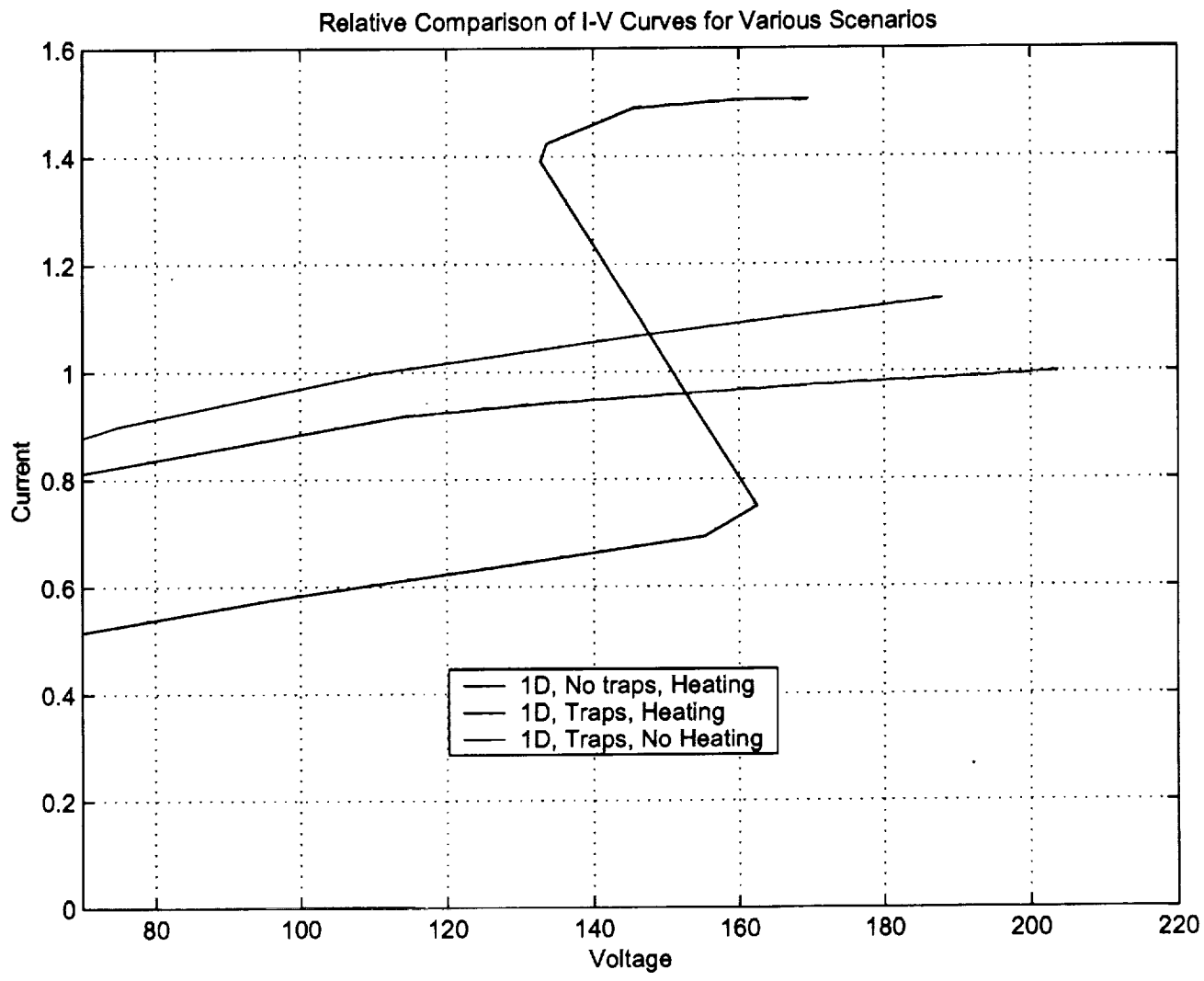


Figure 10

APPENDIX
(PAPER REPRINT)

Analysis of the temperature dependent thermal conductivity of silicon carbide for high temperature applications

R. P. Joshi^{a)}

Department of Electrical and Computer Engineering, Old Dominion University, Norfolk, Virginia 23529-0246

P. G. Neudeck

NASA Glenn Research Center, MS 77-1, 21000 Brookpark Road, Cleveland, Ohio 44135

C. Fazi

U.S. Army Research Laboratory, Adelphi, Maryland 20783

(Received 31 January 2000; accepted for publication 3 April 2000)

The temperature dependent thermal conductivity of silicon carbide has been calculated taking into account the various phonon scattering mechanisms. The results compared very well with available experimental data. The inclusion of four-phonon processes is shown to be necessary for obtaining a good match. Several important phonon scattering parameters have been extracted in this study. Dislocations are shown to have a strong effect at 300 K, but not as much at the higher temperatures.

© 2000 American Institute of Physics. [S0021-8979(00)08513-3]

INTRODUCTION

Silicon carbide (SiC) based electronic devices and circuits are presently being developed for use in high-temperature, high-power, and/or high-radiation conditions under which conventional semiconductors cannot perform adequately.¹⁻⁵ The projected advantages of SiC are associated with its inherent material properties. These include exceptionally high breakdown fields, a large band gap, high electron saturation drift velocities, and large thermal conductivity values. This makes SiC an attractive candidate for devices requiring low leakage currents, high cut-off frequencies at large voltages, in high-temperature electronics, and for high-power microwave operation. Theoretical predictions suggest that SiC power metal-oxide-semiconductor field effect transistors, thyristors, and diode rectifiers would offer significant advantages over their silicon and GaAs counterparts in high-frequency, high-power circuits, and yet require die sizes nearly 20 times smaller.⁶

Despite promising trends, superior quality SiC high-power devices are not being realized presently. While small-area, low-current, low-voltage power SiC devices have successfully been developed, there has been limited progress in the large-area, high-current, high-voltage (i.e., operation near the breakdown field) arena. The presence of a high density of crystallographic defects in commercial SiC wafers (with surfaces perpendicular to the *c* axis), continues to hamper development. Of the various defects, micropipes (i.e., hollow-core screw dislocations) have been the most studied,⁷⁻⁹ and are known to cause premature breakdown point failures at electric fields well below the breakdown threshold. However, with improvements in processing technology, micropipe defect densities have steadily been reduced and are now below 1/cm² in the best prototype wafers.¹⁰ The focus will, there-

fore, naturally begin to shift towards other defects such as elementary, closed-core dislocations. Closed-core screw dislocations are present in all commercial SiC wafers and homoepitaxial layers that are the starting material for SiC electronic devices, due to their nonterminating nature. Densities on the order of thousands/cm² have been reported,^{11,12} and experimental studies of dislocation effects on the electrical behavior are only beginning to emerge. For example, it has recently been demonstrated that screw dislocations can degrade the reverse leakage and breakdown properties of 4H-SiC *p*⁺*n* diodes¹³ and lead to local decreases in carrier lifetimes.¹⁴ In experiments, diodes containing dislocations were shown to exhibit higher pre-breakdown reverse currents, displayed softer breakdown thresholds, and led to the formation of highly localized filamentary microchannels. In light of the above, it becomes important to analyze the impact of dislocations on the response characteristics of SiC devices containing such defects. In a previous study,¹⁵ some of the possible physics behind the electrical behavior were examined. Trapped charge modeled at the dislocation induced defect sites was shown to alter the internal electric field distribution. This, in turn, could affect the ionization rates due to their strongly nonlinear field dependence, and lead to current increases of the SiC diode under reverse bias conditions.

Here, we examine thermal effects in SiC material and the possible role of dislocations on the internal temperature of SiC devices. The thermal issue is especially important for SiC as this material is a primary candidate for high-temperature, high-voltage applications. The electrothermal aspects are also critical in determining the operating limits and boundaries for safe device operation. The thermal conductivity parameter, *k*, depends on an effective phonon relaxation time ϑ_{pr} which is shaped by the combined effects of the various phonon processes.^{16,17} These typically include normal three-phonon processes,^{18,19} boundary scattering,^{20,21}

^{a)}Electronic mail: rpi@sun.engr.odu.edu

isotope/point defect interactions,²² and the umklapp mechanism.^{23,24} If the operating temperatures are not very low, boundary scattering is relatively negligible and the value of k begins to decrease monotonically with temperature due to increases in the combined phonon scattering rate. For bulk SiC, this regime of decreasing thermal conductivity would be encountered for operation at temperatures of 300 K and beyond. Recent experimental studies on 6H-SiC confirm this monotonically decreasing trend in thermal conductivity,²⁵⁻²⁷ and reveal an approximate T^{-n} functional form, with $1 < n < 2$. With such thermal conductivity reductions, device self-heating under high-voltage operation is expected to have a strong influence. Consequences include performance degradation and adverse effects on device stability. It might be mentioned in this regard that there are already reports of filamentary conduction¹³ and device failure in SiC at high bias.²⁸ Although the precise cause remains unclear, internal temperature increases appear to be involved.

Apart from the effects on carrier mobilities and device stability, the device operating temperatures have recently been shown to influence impact ionization rates. Higher ionization coefficients were observed in SiC material containing dislocations and defects, and their values increased with temperature.²⁹ This trend is contrary to that generally seen in silicon and predicted for pure semiconductor materials.³⁰ With increasing temperature, the inelastic phonon scattering increases, making it less likely for a "lucky electron or hole" to remain within the high-energy distribution and subsequently undergo an impact ionizing collision. The ionization rates are thus expected to reduce with increasing temperature. The phenomenon in SiC is not well understood, but is thought to be linked to dislocation physics.^{29,31} We believe charge trapping followed by field- and temperature-assisted detrapping in SiC containing dislocations is a likely cause.¹⁵ In any case, given the temperature sensitivity, it is important to evaluate and characterize the device operating temperatures. Last but not least, the presence of additional phonon scattering at the defects and dislocations in SiC is expected to reduce heat transport, making the thermal issue even more critical. As first pointed out by Klemens,³² the strain fields of screw and edge dislocations contribute to such additional phonon scattering. This can lead to reductions in thermal conductivity, as has been observed experimentally in SiC (Ref. 33) and other materials.³⁴

In light of the above, a thermal analysis for SiC devices becomes relevant and germane. In this article, the temperature dependence of SiC thermal conductivity has been probed taking into account the various phonon scattering mechanisms. The results are carefully compared with available experimental data, and found to be in very good agreement. In the process of such a comparison, several important parameters associated with the various phonon processes have been extracted in this study. Finally, the role of dislocation scattering and associated thermal conductivity reductions is also discussed.

SIMULATION DETAILS

We begin by focusing on the thermal conductivity parameter, $k(T)$, and providing some relevant comments with

regard to its expected temperature dependence and the role of various constituent phonon scattering processes. As already mentioned, recent experimental data on 6H-SiC has yielded the following temperature dependent expression:²⁶ $k(T) = 4.517 \times 10^5 T^{-1.29} \text{ W m}^{-1} \text{ K}^{-1}$. This temperature dependence is dictated by the collective contribution of several phonon scattering mechanisms. To the best of our knowledge, the relative role of the constituent scattering processes has not been analyzed, nor have the parameters associated with the interactions been extracted for SiC. Furthermore, the measurements were made on actual samples, which might or might not have been relatively defect free. This point has not been explicitly stated or clarified in Ref. 26, so it needs to be examined. The presence of a high-density network of basal plane dislocations, often reported in SiC wafers, could reduce thermal conductivity. Here, we have carried out a theoretical analysis to probe some of the thermal conductivity issues based on the theory developed by Callaway¹⁶ and by Slack and co-workers.²⁴ The following assumptions have implicitly been made. (1) Phonons transport all of the heat. Hence, electronic contributions or radiation transport are neglected. Justification is partially based on a recent study that confirms the weakness of these processes in SiC.²⁶ (2) The phonons can be represented by a Debye-type approximation with a single frequency-independent phonon velocity, and a maximum frequency fixed by the Debye temperature. Although the presence of defects produces variations in the atomic mass and force constants, thereby changing the phonon spectra, this effect has been neglected here. (3) Anisotropic effects have also been ignored. (4) The relaxation time approximation has been used for simplicity since expressions for the individual relaxation processes are well known. (5) It has been assumed that contributions from the normal processes (i.e., momentum conserving) can be ignored in the temperature range of 300–800 K that is of interest for the present calculations. This range was chosen so as to remain below the 1200 K Debye temperature for SiC.

Basically, the thermal conductivity can be expressed in terms of the effective phonon relaxation time ϑ_{pr} and is given as¹⁶

$$k(T) = (4\pi k_B / v_s) (k_B T / h)^3 \times \int_0^{\theta/T} x^4 \vartheta_{pr}(x) [e^x / (e^x - 1)^2] dx, \quad (1)$$

where θ is the Debye temperature, v_s the average velocity of sound, h is Planck's constant, k_B the Boltzmann constant, and $x = (h\omega) / (2\pi k_B T)$. The phonon time ϑ_{pr} in the above equation can roughly be obtained based on the relaxation time approximation (RTA). In the RTA, each phonon scattering mechanism is treated as making a separate and independent contribution to the overall relaxation rate ϑ_{pr}^{-1} . Thus, in terms of the i th scattering mechanism, the following equation results:

$$\vartheta_{pr}^{-1} = \sum_i \vartheta_i^{-1} = \vartheta_i^{-1} + \vartheta_U^{-1} + \vartheta_D^{-1} + \vartheta_B^{-1} + \vartheta_N^{-1} + \vartheta_{4P}^{-1}, \quad (2)$$

where ϑ_I , ϑ_U , ϑ_D , ϑ_B , ϑ_N , and ϑ_{4P} are the relaxation times associated with isotope scattering, the Umklapp process, dislocation scattering, the phonon-boundary interactions, normal phonon processes, and four-phonon events, respectively. Of these, the normal processes do not significantly affect the thermal conductivity much since the phonon momentum is conserved. Hence, their contribution has been neglected in this treatment. The four-phonon processes, as suggested by Pomerranchuk,³⁵ play a role at high temperatures, and have been considered here. As the results will show, the four-phonon process appears to be fairly important in SiC, and good agreement with experimental data cannot be obtained without its inclusion. Applying the well known expressions to the processes^{16,22} leads to the following mathematical expressions for the scattering rates: $\vartheta_I^{-1} = A\omega^4$, $\vartheta_U^{-1} = BT \exp[-\theta/(aT)]\omega^2$, $\vartheta_B^{-1} = v_s/L$, $\vartheta_D^{-1} = DN_D b^2 \omega$, and $\vartheta_{4P}^{-1} = CT^2 \omega^2$, where A , B , C , and D are material constants. The parameter ‘‘a’’ for the Umklapp process is adjustable. Previous reports on several semiconductor materials suggest that the $1 \leq a \leq 3$ range yields a good fit to experimental data.²⁴ For SiC, a value of $a=1$ has been used recently by Muller *et al.*²⁶ As pointed out by Klemens,²² if a number of parallel dislocations are grouped together in a region whose spatial extent is small compared to the phonon wavelength, their scattering can be reinforced. The overall effect can then be treated as a single dislocation having a Burgers vector given by the sum of individual dislocations. Numerically, this can be folded into the D parameter given above. The overall effective phonon relaxation time thus has the following general form:

$$\vartheta_I^{-1} = A\omega^4 + BT \exp[-\theta/(aT)]\omega^2 + CT^2 \omega^2 + DN_D b^2 \omega + v_s/L, \quad (3)$$

where L is the characteristic length scale of the sample, ω the phonon frequency, N_D the dislocation density per unit area, and b the magnitude of the Burgers vector. Using Eq. (3) in Eq. (1) then leads to the following conductivity expression:

$$k(T) = [4\pi k_B/v_s](k_B T/h)^3 \int_0^{\theta/T} \{x^4/[P_1 x^4 + (P_2 + P_3)x^2 + P_4 x + v_s/L]\} [e^x/(e^x - 1)^2] dx, \quad (4)$$

where $P_1 = A(2\pi k_B T/h)^4$, $P_2 = BT^3 \exp[-\theta/(aT)] \times (2\pi k_B/h)^2$, $P_3 = CT^2(2\pi k_B T/h)^2$, and $P_4 = DN_D b^2 \times (2\pi k_B T/h)$. It is perhaps instructive to examine the expected behavior of $k(T)$ at high temperatures. At 300 K and beyond, the $x^2[e^x/(e^x - 1)^2]$ term approaches unity. Also, as is well known, the boundary scattering becomes negligibly small. Equation (4) then yields

$$k(T) = [4\theta k_B/v_s](k_B T/h)^3 \times \int_0^{\theta/T} \{x^2/[P_1 x^4 + (P_2 + P_3)x^2 + P_4 x]\} dx. \quad (5)$$

In the absence of dislocation scattering, the above equation works out to

TABLE I. Parameters used for thermal conductivity calculations for SiC.

Parameter	Value
Debye temperature (K)	1.2×10^3
Acoustic velocity (m s^{-1})	1.3×10^4
Boundary scattering length L (m)	0.5×10^{-2}
Isotope scattering parameter A (s^3)	8.46×10^{-45}
Umklapp parameter B (s K^{-1})	6.1626×10^{-20}
Parameter b for umklapp process	1.0
Four-phonon process parameter C (s K^{-2})	6.9×10^{-23}
Burgers vector b (m)	14.5×10^{-10}

$$k(T) \sim T^{-0.5} \{C_1 \exp[-\theta/(aT)] + C_2 T\}^{-0.5} \times \tan^{-1} \{ \theta [C_1 T \exp[-\theta/(aT)] + C_2 T^2]^{0.5} \} \sim T^{-0.5} \{C_1 \exp[-\theta/(aT)] + C_2 T\}^{-0.5}, \quad (6)$$

where C_1 and C_2 are temperature independent constants and arise from factors P_2 and P_3 . Neglecting the C_1 factor leads roughly to a $k(T) \sim T^{-1}$ dependence. However, the actual variation is more complicated since the C_1 factor cannot really be neglected since the umklapp processes are quite important. The umklapp process dominance is demonstrated and discussed through numerical computations next. A larger negative exponent value is predicted for the temperature dependence based on Eq. (6) above. Recent experimental reports of the SiC thermal conductivity suggest a $T^{-1.29}$ temperature variation.²⁶ Since this is close to the approximate analysis discussed above, it is reasonable to conclude that dislocation scattering in the experimental samples was either weak or absent. A numerical analysis that will be presented next shows that good agreement with the experimental data can be achieved without any considerations of the dislocation scattering mechanism. As a final point, data are currently not available for the 4H-SiC polytype. However, one could use Eq. (4) to go from the 6H-SiC to the 4H-SiC parameters. Very roughly, the values would be related to the inverse ratio of the acoustic velocities. Since $v_s|_{4H} \sim v_s|_{6H} = 1.3 \times 10^4 \text{ m s}^{-1}$, the same $k(T) = 4.517 \times 10^5 T^{-1.29} \text{ W m}^{-1} \text{ K}^{-1}$ expression can roughly be used for the 4H-SiC thermal conductivity as well.

RESULTS AND DISCUSSION

Numerical calculations for the thermal conductivity were carried out based on Eq. (4). Since not all of the scattering parameters are well known for SiC, the intent was to obtain reasonable fitting values for all the parameters through direct comparisons between theory and the available experimental data. In the process, the role of constituent phonon scattering mechanisms was brought out very clearly. Only some of the parameter values for the phonon scattering times are known from the literature.^{36,37} Others had to be adjusted in order to achieve a good fit with the experimental data. The overall set of parameters that emerged and were used here are given in Table I. Dislocation scattering was deliberately ignored to begin with. The intent was to ascertain whether it would be possible to achieve a reasonable match with the available

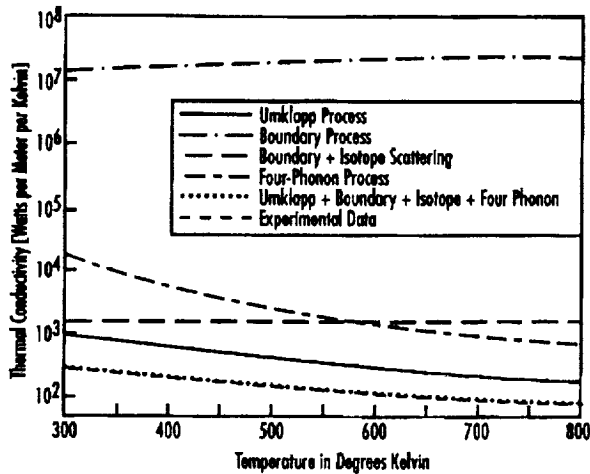


FIG. 1. Simulation results of the temperature-dependent SiC thermal conductivity resulting from a variety of phonon scattering mechanisms. An experimental curve (after Ref. 26) is also shown.

experimental data without the dislocation scattering mechanism. Good agreement would either indicate an absence of dislocations in the experimental samples, or a relatively weak contribution from this scattering process. Figure 1 shows the calculated SiC thermal conductivity associated with the various constituent phonon scattering mechanisms. Experimental data are also given for the 300–800 K range. The comprehensive result reveals a rather good match with the available SiC data. The umklapp process is evidently the strongest in this entire temperature regime. The isotope/defect mechanism is the next most dominant process near room temperature, but is overtaken by four-phonon scattering beyond 600 K. The role of four-phonon scattering, which has been ignored in many previous studies, is brought out more clearly in Fig. 2. Without the four-phonon process, the thermal conductivity resulting from all of the remaining mechanisms is predicted to be much larger than the measured data. In addition, the slope is substantially incorrect in

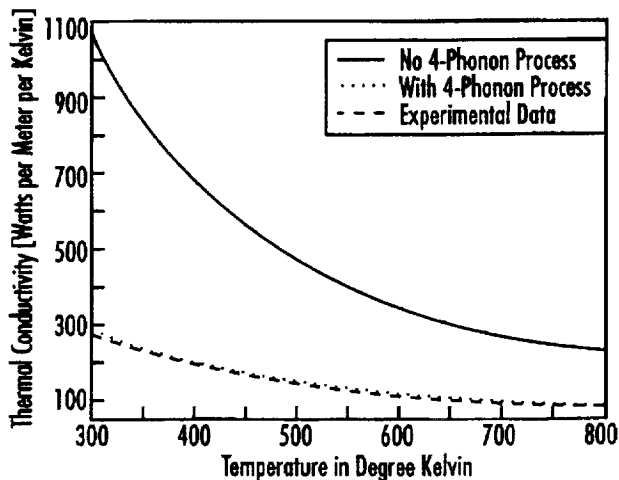


FIG. 2. Simulation predictions of the temperature-dependent SiC thermal conductivity with and without the four-phonon processes being taken into account. Experimental data are shown for comparison.

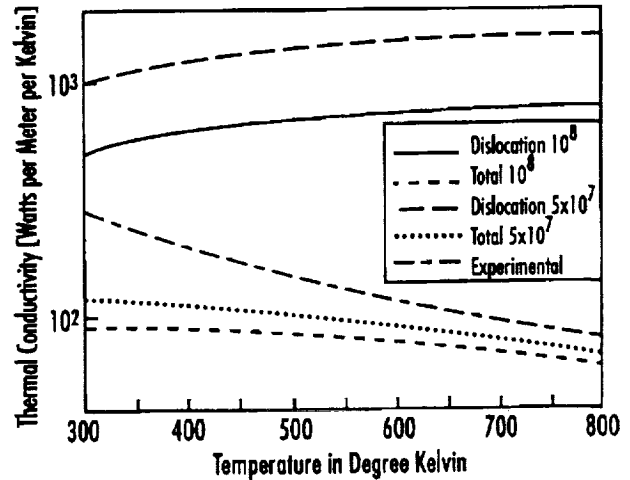


FIG. 3. Predictions of the temperature-dependent thermal conductivity using two values of the dislocation parameter R . Experimental data are also shown.

the absence of the four-phonon processes, especially at the lower temperatures. Close agreement between theoretical predictions and the data curve underscores the weakness of dislocation scattering. The role of dislocation scattering is not negated though, since the result might simply have been the consequence of using relatively pure samples in the actual experiments of Muller *et al.*²⁶

In order to roughly assess the effect of dislocations on thermal conductivity, the preceding calculations were repeated but with inclusion of the dislocation scattering term. Parameter values for the remaining processes were kept fixed as given in Table I. The P_4 term of Eq. (4) was treated as a variable. Thus denoting $P_4 = [DN_D b^2 (2Bk_B/h)]T \equiv RT$, the temperature-dependent SiC thermal conductivity was obtained for two values of the parameter R . The corresponding curves are shown in Fig. 3 for two values of R : $R = 5 \times 10^7$ and $10^8 \text{ s}^{-1} \text{ K}^{-1}$. The thermal conductivity in Fig. 3 due to the dislocations alone exhibits a monotonic increase with temperature. This trend is opposite that exhibited by all the remaining processes, and demonstrates that dislocation scattering is expected to have an impact primarily at the lower operating temperatures. The total thermal conductivity, taking into account all of the remaining phonon processes, has a value lower than the experimental baseline result, and exhibits a reduced temperature variation. Thermal conductivities as low as $95 \text{ W m}^{-1} \text{ K}^{-1}$ are predicted in Fig. 3 for room temperature operation. The technological implications are obvious. Dislocations lead to the formation of defect states due to internal lattice strain. Charge trapping at these sites can then give rise to S -shaped negative differential conductance characteristics³⁸ and trigger devices into a filamentary mode. High current densities in such filaments, coupled with the strong conductivity decreases with temperature as predicted here, could lead to catastrophic and irreversible failures in SiC devices.

CONCLUSIONS

The temperature dependence of SiC thermal conductivity has been probed in this study taking account of the vari-

ous phonon scattering mechanisms. The process of phonon scattering at screw dislocations due to the internal lattice strain has been included. Such calculations have not been performed previously to the best of our knowledge. It has been demonstrated that the dislocations are likely to affect the thermal conductivity adversely at the lower temperatures. The simulation results were carefully compared with available experimental data, and found to be in very good agreement. The inclusion of four-phonon processes was shown to be necessary for obtaining a good match. In the process of such a comparison, several important parameters associated with the various phonon processes have been extracted in this study.

The role of dislocation scattering was shown to be quite strong at the room temperature value. The implications for technological development of SiC devices are obvious. Structures having screw dislocations should be avoided not only because they reduce the thermal conductivity, but also because they can initiate filamentary conduction, leading to large localized temperature increases.

ACKNOWLEDGMENTS

The authors would like to acknowledge fruitful discussions with W. Choyke (University of Pittsburgh). Partial support from NASA Glenn Research Center is gratefully acknowledged. This work was also sponsored in part by the Army Research Laboratory.

- ¹P. G. Neudeck, *J. Electron. Mater.* **24**, 283 (1995).
- ²M. Bhatnagar and B. J. Baliga, *IEEE Trans. Electron Devices* **40**, 645 (1993).
- ³R. J. Trew, J. Yan, and P. M. Mock, *Proc. IEEE* **79**, 598 (1991).
- ⁴P. A. Ivanov and V. E. Chelnokov, *Semicond. Sci. Technol.* **7**, 663 (1992).
- ⁵H. Morkoç, S. Strite, G. B. Gao, M. E. Lin, B. Sverdlov, and M. Burns, *J. Appl. Phys.* **76**, 1363 (1994).
- ⁶B. J. Baliga, *IEEE Spectr.* **32**, 34 (1995).
- ⁷P. G. Neudeck and J. A. Powell, *IEEE Electron Device Lett.* **15**, 63 (1994).
- ⁸S. V. Rendakova, I. P. Nikitina, A. Tregubova, and V. Dmitriev, *J. Electron. Mater.* **27**, 292 (1998).
- ⁹J. W. Palmour, L. A. Lipkin, R. Singh, D. B. Slater, Jr., A. V. Suvorov, and C. H. Carter, Jr., *Diamond Relat. Mater.* **6**, 1400 (1997).
- ¹⁰V. F. Tsvetkov, R. C. Glass, D. Henshall, D. A. Asbury, and C. H. Carter, Jr., *Mater. Sci. Forum* **264–268**, 3 (1998).
- ¹¹P. G. Neudeck, W. Huang, and M. Dudley, in *Power Semiconductor Materials and Devices*, edited by S. J. Pearton, R. J. Shul, E. Wolfgang, F. Ren, and S. Tenconi (Materials Research Society, Warrendale, PA, 1998), Vol. 483, pp. 285–294.
- ¹²S. Wang, M. Dudley, C. H. Carter, Jr., V. F. Tsvetkov, and C. Fazi, in *Applications of Synchrotron Radiation Techniques to Materials Science*, edited by L. Terminello, N. Shinn, G. Ice, K. D'Amico, and D. Perry (Materials Research Society, Warrendale, PA, 1998), Vol. 375, pp. 281–286.
- ¹³P. G. Neudeck, W. Huang, and M. Dudley, *IEEE Trans. Electron Devices* **46**, 478 (1999).
- ¹⁴C. M. Schnabel, M. Tabib-Azar, P. G. Neudeck, S. G. Bailey, H. B. Su, and M. Dudley, *Mater. Sci. Forum* (in press).
- ¹⁵L. Zheng, R. P. Joshi, and C. Fazi, *J. Appl. Phys.* **85**, 7935 (1999).
- ¹⁶J. Callaway, *Phys. Rev.* **113**, 1046 (1959); **122**, 787 (1961).
- ¹⁷J. Callaway and H. C. von Baeyer, *Phys. Rev.* **120**, 1149 (1960).
- ¹⁸C. Herring, *Phys. Rev.* **95**, 954 (1954).
- ¹⁹P. G. Klemens, in *Encyclopedia of Physics*, edited by S. Flugge (Springer, Berlin, 1956), Vol. 14, p. 198.
- ²⁰W. J. de Haas and T. Biermasz, *Physica (Amsterdam)* **5**, 619 (1938).
- ²¹R. Berman, *Proc. R. Soc. London, Ser. A* **208**, 90 (1951).
- ²²P. G. Klemens, in *Solid State Physics*, edited by F. Seitz and D. Turnbull (Academic, New York, 1958), Vol. 7, p. 1.
- ²³R. Peierls, *Ann. Phys. (Leipzig)* **3**, 1055 (1929).
- ²⁴G. A. Slack and S. Galginaitis, *Phys. Rev.* **133**, A253 (1964); C. J. Glassbrenner and G. A. Slack, *ibid.* **134**, A1058 (1964).
- ²⁵E. Jansen, R. Ziermann, E. Obermeier, G. Krotz, and Ch. Wagner, *Mater. Sci. Forum* **264–268**, 631 (1998).
- ²⁶St. Muller, R. Eckstein, J. Fricke, D. Hofmann, R. Hofmann, R. Horn, H. Mehling, and O. Nilsson, *Mater. Sci. Forum* **264–268**, 623 (1998).
- ²⁷D. Morelli, J. P. Heremans, C. P. Beetz, W. S. Yoo, and H. Matsunami, *Appl. Phys. Lett.* **63**, 3143 (1993).
- ²⁸P. G. Neudeck and C. Fazi, *J. Appl. Phys.* **80**, 1219 (1996).
- ²⁹R. Raghunathan and B. J. Baliga, *Appl. Phys. Lett.* **72**, 3196 (1998).
- ³⁰C. R. Crowell and S. M. Sze, *Appl. Phys. Lett.* **9**, 242 (1966).
- ³¹A. G. Chynoweth and G. L. Pearson, *J. Appl. Phys.* **29**, 1103 (1958).
- ³²P. G. Klemens, *Proc. R. Soc. London, Ser. A* **208**, 108 (1951); *Proc. Phys. Soc., London, Sect. A* **68**, 1113 (1955).
- ³³G. A. Slack, *J. Appl. Phys.* **35**, 3460 (1964).
- ³⁴R. L. Sproull, M. Moss, and H. Weinstock, *J. Appl. Phys.* **30**, 334 (1959).
- ³⁵I. Pomerranchuk, *Phys. Rev.* **60**, 820 (1941); *J. Phys. (Moscow)* **4**, 259 (1941); **6**, 237 (1941).
- ³⁶See, for example, O. Madelung, *Physics of Group IV Elements and III-V Compounds, Group III*, Landolt-Bornstein New Series, Vols. 17a and 22a (Springer, Berlin, 1981).
- ³⁷I. I. Parfenova, Y. M. Tairov, and V. F. Tsvetkov, *Sov. Phys. Semicond.* **24**, 158 (1990).
- ³⁸See, for example, M. Shaw, V. V. Mitin, E. Scholl, and H. L. Grubin, *The Physics of Instabilities in Solid State Devices* (Plenum, New York, 1992).